Statistical Parameters of the Air Turbulent Boundary Layer over Steep Water Waves Measured by the PIV Technique

YU. TROITSKAYA, D. SERGEEV, O. ERMAKOVA, AND G. BALANDINA

Institute of Applied Physics, Russian Academy of Sciences, Nizhny Novgorod, Russia

(Manuscript received 27 October 2009, in final form 24 February 2011)

ABSTRACT

A turbulent airflow with a centerline velocity of 4 m s^{-1} above 2.5-Hz mechanically generated gravity waves of different amplitudes has been studied in experiments using the particle image velocimetry (PIV) technique. Direct measurements of the instantaneous flow velocity fields above a curvilinear interface demonstrating flow separation are presented. Because the airflow above the wavy water surface is turbulent and nonstationary, the individual vector fields are conditionally averaged sampled on the phase of the water elevation. The flow patterns of the phase-averaged fields are relatively smooth. Because the averaged flow does not show any strongly nonlinear effects, the quasi-linear approximation can be used. The parameters obtained by the flow averaging are compared with the theoretical results obtained within the theoretical quasi-linear model of a turbulent boundary layer above the wavy water surface. The wave-induced pressure disturbances in the airflow are calculated using the retrieved statistical ensemble of wind flow velocities. The energy flux from the wind to waves and the wind–wave interaction parameter are estimated using the obtained wave-induced pressure disturbances. The estimated values of the wind–wave interaction parameter are in a good agreement with the theory.

1. Introduction

Small-scale air–sea interaction is one of the most important factors determining the exchange processes in the air–sea boundary layers (i.e., wind stress, heat, and mass exchange between the atmosphere and the ocean). These processes govern the boundary conditions for the atmosphere and the ocean and affect the coupled dynamics of both geospheres. Therefore, parameterization of the exchange processes on the air–sea interface is of special interest, particularly with the view of improving the climate and weather prediction models, investigation of the sea–air interaction under severe wind, tropical hurricanes, etc.

Another important aspect of the air–sea interaction is excitation of surface waves. One of the most debated issues of wave modeling is concerned with the wind input in the wave field. Two physical mechanisms of wind excitation of small-amplitude waves have been suggested so far. In the first, quasi-laminar Miles (1957, 1959) mechanism, wind wave generation is conditioned by the resonance energy exchange in the critical layer. The effect of viscous stresses in the wind flow running faster than the wave is responsible for the second mechanism described in terms of molecular viscosity (Miles 1962), eddy viscosity (Miles 1965; Gent 1977; Gent and Taylor 1976; Al-Zanaidi and Hui 1984), or the rapid distortion theory (Belcher and Hunt 1993; Miles 1996; Ierley and Miles 2001). Theoretical models of the finite-amplitude wave excitation by wind were proposed by Janssen (1991), van Duin and Janssen (1992), Jenkins (1992), and Reutov and Troitskaya (1995) on the basis of the quasi-linear approximation when the wave-induced disturbances in the airflow are described in the linear approximation, but the nonlinear effect of the mean wind velocity deformation due to the radiation force (the impact of the wave momentum flux) is taken into account. These theoretical models based on the semiempirical models of turbulence in the wind presume a nonseparating regime of airflow over waves. It should be emphasized that, in the cited papers, the hypothesis on the absence of flow separation concerned the velocity fields averaged over turbulent fluctuations.

An alternative physical hypothesis on the wind wave excitation due to airflow separation at the crest of the

Corresponding author address: Dr. Yuliya Troitskaya, Institute of Applied Physics, Russian Academy of Sciences, Ulyanov str., 46, 603950 Nizhny Novgorod, Russia.
E-mail: yuliya@hydro.appl.sci-nnov.ru

DOI: 10.1175/2011JPO4392.1

wave was advanced by Jeffreys (1924, 1925) 85 years ago, but it was neither confirmed nor rejected up to now. One can expect existence of strong nonlinear phenomena (sheltering, flow separation, etc.) for the cases of steep and breaking waves. These phenomena were investigated by means of contact methods and smoke visualization in the laboratory experiments by Banner and Melville (1976), Kawamura and Toba (1988), Kawai (1981, 1982), Hsu et al. (1981), and Papadimitrakis et al. (1984). Major difficulties in those experiments were concerned with measuring the airflow close to the water surface, especially in the wave troughs. Such measurements can be performed by means of the wave-following contact technique (Hsu et al. 1981; Papadimitrakis et al. 1984; Donelan et al. 2005). Also, the problem of measuring wind flow below wave crests was solved by Kawai (1981, 1982), who seeded the flow with small particles visualized with a strobe source of light and used a special photo technique. Kawai's experiments demonstrated airflow separation from the crests of steep waves in instant images of the flow.

The structure of an airflow over waves was investigated in detail by the method of particle image velocimetry (PIV) (Adrian 1991), when the flow is seeded with small particles illuminated by laser light and then recorded by a digital camera. This technique was used by Reul et al. (1999, 2008) and Veron et al. (2007) and clearly demonstrated the effect of airflow separation from wave crests and reattachment at the windward face of the wave in the instantaneous patterns of vector velocity fields. It should be emphasized that the PIV technique provides an instant picture of the velocity field, but the flow separation in the turbulent boundary layer over a gravity wave is a strongly nonstationary process because of both the stochastic character of the airflow and the brevity of the breaking event, which usually occurs within a small part of the wave period (Duncan et al. 1999). At the same time, the models of the air–sea fluxes and wind wave growth exploit the wind flow parameters averaged over turbulent fluctuations. In this paper, we proposed an approach for investigation of aerodynamic fields over surface waves that combines measurement of instant airflow velocity fields with statistical averaging. A statistical ensemble of such vector fields for subsequent averaging was obtained by means of high-speed video filming and processing of the video films by the PIV algorithm. The mean velocity fields were then obtained by subsequent conditional averaging of the measured vector fields over the phase of water wave elevation. The rate of the video shooting, specified by the spatial resolution of the data processing algorithm (see section 2), was chosen to be 1000 frames per second.

These mean velocity fields in the airflow over waves, obtained by conditional averaging of the individual vector fields, were found to be smooth even for steep and breaking waves, whereas the individual vector fields manifested irregularities and signs of flow separation. In the subsequent processing of the statistical ensemble of the airflow velocity vector fields, averaged and wave-induced velocity components and turbulent stresses were retrieved. These quantities allowed calculating the wave disturbances of the pressure field based on generalization of the integral expressions from the paper by Benjamin (1959) (see section 3b), which in turn enabled estimating the energy flux from wind to wave and the wind–wave interaction parameter. The results of the measurements were compared with the calculations within the quasi-linear model proposed by Reutov and Troitskaya (1995).

This paper has the following architecture: In section 2, the experimental setup and the details of the PIV algorithm for continuous video shooting are described. In section 3, the procedure of data processing is presented, including construction of time series, ensemble averaging, reference frame, and curvilinear coordinates used for data presentation. The algorithm of retrieving the pressure field from the ensemble of turbulent velocity fields is discussed in detail. In section 4, the ensemble-averaged water surface elevation field and the drift flow in the water are considered. In section 5, the ensemble-averaged aerodynamic fields in the airflow over waves are analyzed, including the parameters of the velocity field (section 5a) and the pressure field (section 5b). The quasi-linear model of turbulent wind over a wavy water surface is presented in section 6, and in section 7 the experimental data are compared with the predictions of the theoretical model.

2. Experimental setup

a. Wind–wave circular tank

The experiments on a turbulent airflow above a wavy water surface were conducted in the wind–wave circular tank of the Institute of Applied Physics of the Russian Academy of Sciences (IAP RAS; see Fig. 1). The tank consists of two semicircumferences with diameters of 4 m, linked with 2-m-long straight sections; the overall length of the tank is 16 m. Its cross section is 30 cm wide and 59 cm high. Rectangular windows 50 cm high and 45 cm wide are located on both sides of the straight sections. The water depth in the tank is 32 cm. A wind-generating fan is installed at the semicircular–straight section junction. To decrease the fluctuations of the flow a honeycomb is placed next to the fan. For investigating

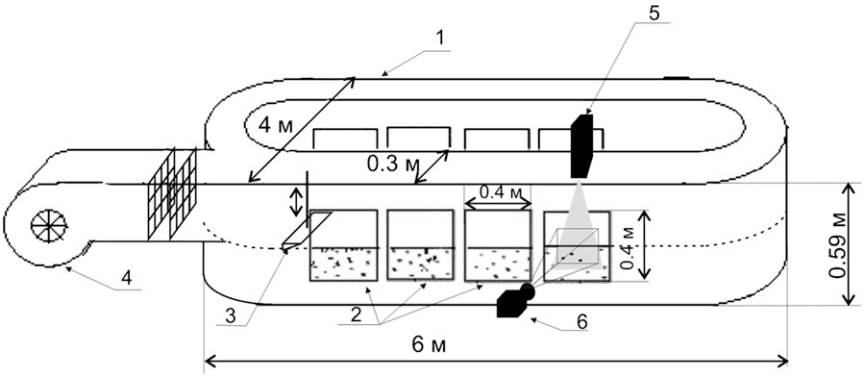

FIG. 1. Experimental setup: 1) the circular glass-windowed wind–wave tank (16 m long and 0.3 m wide with the water depth of 0.32 m); 2) the rectangular windows (45×50 cm^2); 3) the wedge-shape surface wavemaker; 4) the fan; 5) the 532-nm, 0.5-W Nd:Yag laser; and 6) the high-speed video camera Videoscan VS-FAST (1000 frames s^{-1}, 1280×500 pixels).

the properties of the mean wind profiles in the visualized area mean horizontal wind velocity was measured using hot-wire anemometers, the centerline airflow velocity in the wind–wave tank was 4 m s^{-1}.

The surface waves in the tank were generated in the upwind end of the tank with a programmable wedge-shape wavemaker ($29.5 \times 8 \times 3.5$ cm^3), located at a distance of 30 cm from the fan. It was oscillating vertically with the amplitudes of 6.5, 14, and 20 mm, being driven by the input harmonic signal from the generator with the frequency of 2.5 Hz (the period of 400 ms).

The test window (Fig. 2) was located at 3-m fetch from the fan. The frequency spectra of the waves generated by the wavemaker in the absence and in the presence of airflow measured by the resistive wave gauge are plotted in Figs. 3a,b, respectively. One can see that the airflow leads to widening of the wave spectra generated by the wavemaker. The effect is more pronounced for the waves of large amplitudes (cases 2 and 3), which is possibly associated with the enhancement of wave breaking observed in video.

b. *Experimental setup for the airflow PIV*

Measurements of the instantaneous airflow velocity fields were made with the PIV technique. The entire region from the water surface to the top boundary of the frame filmed by a charge-coupled device (CCD) camera was seeded with almost spherical polyamide particles 20 μm in diameter. The particles were injected into the airflow by compressed air passed through a special device, a hollow vertical tube 8 mm in diameter with circular holes 1.5 mm in diameter on the sidewall of the tube at a distance of 5 mm from each other. The injection device was placed 35 cm from the boundary of the visualization area.

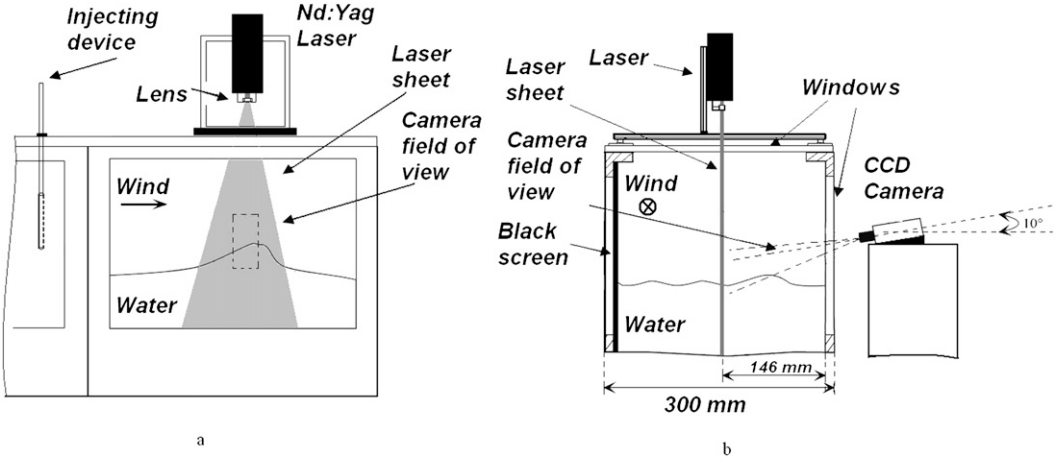

FIG. 2. The experimental setup in the working section: (a) front view and (b) side view.

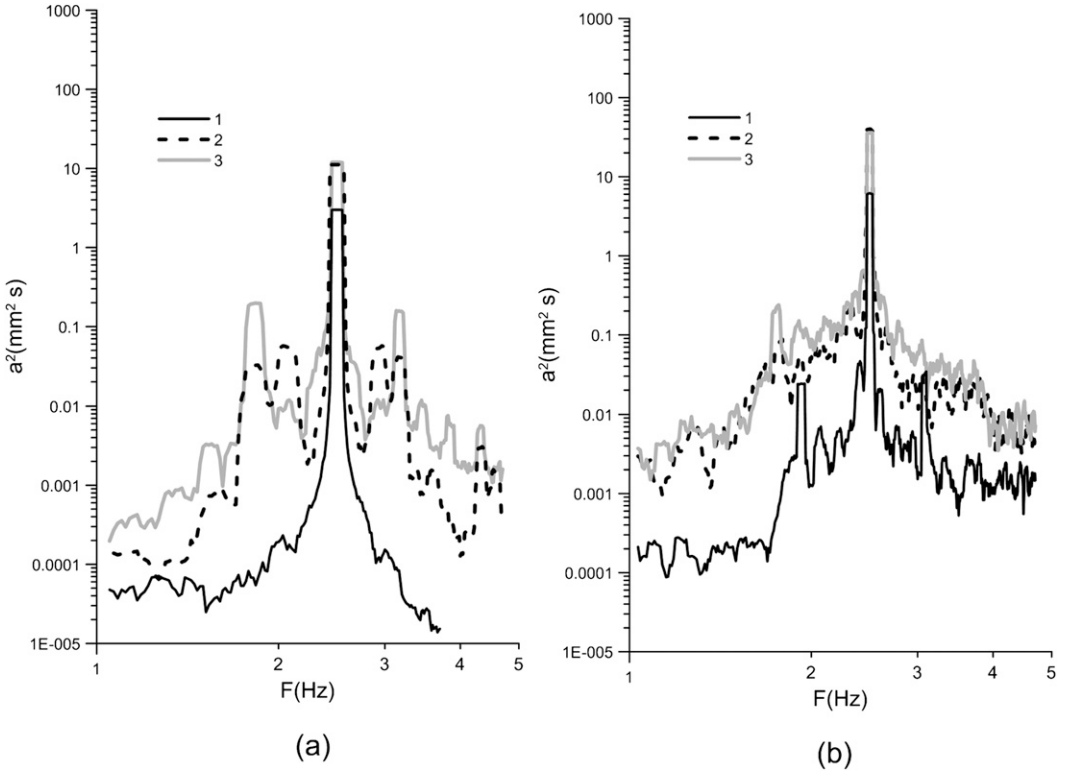

FIG. 3. The frequency spectra of surface waves generated (a) by the wavemaker and (b) by the wavemaker and the airflow for the wavemaker amplitudes 1–6.5 mm, 2–14 mm, and 3–20 mm.

Undesirable disturbances introduced to the airflow by the injection device may be classified as follows:

1) the wake past the body of the device, or
2) disturbances due to injection of compressed air.

Special test experiments were performed to estimate these disturbances. Mean velocity and turbulent shear stress profiles over a smooth surface were measured by the PIV method in the presence of the model of the injection device installed in 35 cm upwind from the working area and without it. It was shown that the difference between horizontal velocities caused by the wake flow past the injection device in the area of PIV measurements was less than 8% (see Fig. 4a) and the estimates of logarithmic derivatives in both cases differs in about 5%. It is in a good agreement with the turbulent stress profiles plotted in Fig. 4b, where essential difference occurs only at the distance more than 30–35 cm from the surface, so it was possible to neglect the distortions caused by the wake behind the injection device.

The injection device uses compressed air for infusing particles into an ambient airflow, which results in undesirable disturbance of the flow velocity near the nozzle of the device. The distance from the nozzle where the disturbance is essential may be estimated as follows. The relaxation time of the disturbance with scale L in a turbulent flow can be estimated as $T_{\text{rel}} = L^2/\nu_{\text{turb}}$, where $\nu_{\text{turb}} = \kappa u_* z$ is the eddy viscosity coefficient in the turbulent boundary layer. The scale of relaxation of the disturbance downstream can be estimated as $X_{\text{rel}} = T_{\text{rel}} U_i = U_i L^2/\nu_{\text{turb}}$, where U_i is the mean velocity of translation of the disturbance caused by the ambient flow. Taking into account that $L = 0.1$ cm (the diameter of a single hole of the injection device), $U_i = 10$ m s^{-1} is the speed of injection, the friction velocity $u_* = 20$ cm s^{-1} (see Table 2), we have $X_{\text{rel}} = 2.5$ mm. These estimations show that the airflow disturbance caused by the injection device will not affect the flow field in the working window.

To quantify the inertial effect of the particles, we consider the motion of a spherical particle with diameter $d = 20$ μm, injected with initial velocity U_i into the airflow with undisturbed velocity vector field $\mathbf{U}_f$ in the gravity field. In the Stokes approximation, the motion of a small spherical particle with density ρ_p in the airflow with density ρ_a is governed by the following equation:

$$\rho_p \frac{\pi}{6} d^3 \frac{d\mathbf{U}_p}{dt} = -3\pi d \nu_a \rho_a (\mathbf{U}_p - \mathbf{U}_f) + \rho_p \frac{\pi}{6} d^3 \mathbf{g}, \qquad (2.1)$$

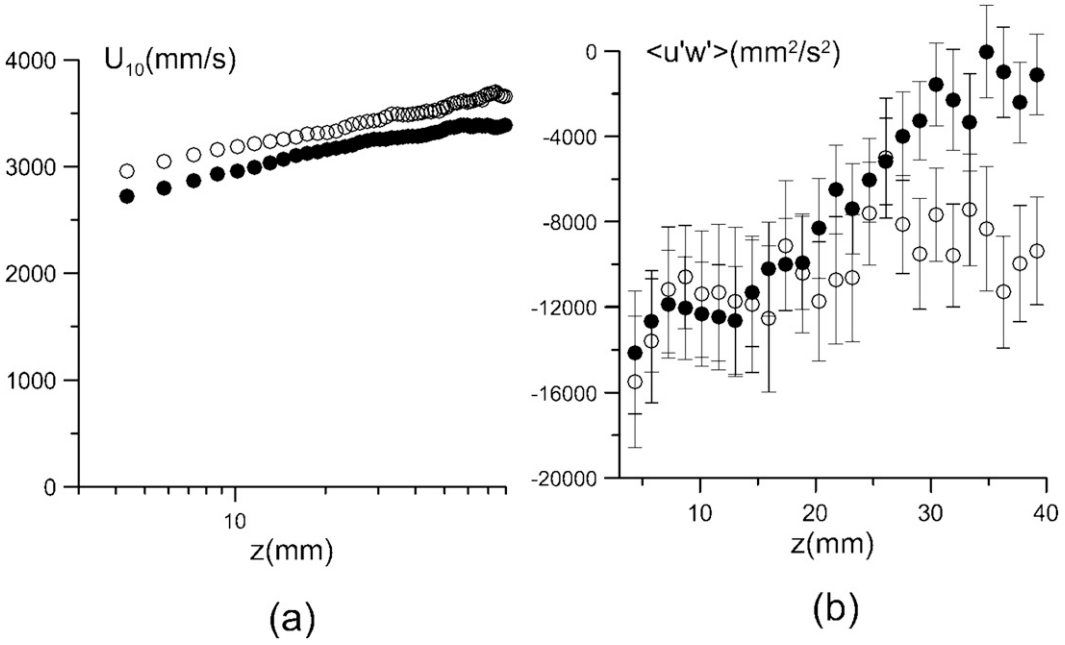

FIG. 4. (a) Mean horizontal velocity and (b) turbulent shear stress profiles in the working window measured by the PIV technique with injecting device (closed circles) and without injecting device (open circles).

with the initial conditions

$$\mathbf{U}_p|_{t=0} = \mathbf{U}_i. \tag{2.2}$$

Here, ν_a is the kinematic viscosity of air and g is the acceleration due to gravity.

Suppose for simplicity of the estimations that $\mathbf{U}_f$ is a constant vector, then Eq. (2.1) can be easily integrated, yielding for the particle velocity in the horizontal direction,

$$U_{p||} = U_{f||} + (U_{i||} - U_{f||}) \exp(-t/\tau), \tag{2.3}$$

and in the vertical direction,

$$U_{p\perp} = (U_{f\perp} - g\tau)[1 - \exp(-t/\tau)]. \tag{2.4}$$

Here, $\tau = (\rho_{\text{part}}/\rho_{\text{air}})(d^2/18\nu_a)$ is the inertial time of the particles, for the parameters of this experiment $\rho_p = 1.02$ g cm^{-3}, $\rho_{\text{air}} = 1.25 \times 10^{-3}$ g cm^{-3}, $d = 2 \times 10^{-3}$ cm, $\nu_a = 0.15$ cm^2 s^{-1}, and $\tau = 1.2 \times 10^{-3}$ s.

The distance x passed by a particle along the flow can be found by integrating Eq. (2.3) over time,

$$x = U_{f||}t + (U_{i||} - U_{f||})\tau[1 - \exp(-t/\tau)] \tag{2.5}$$

The horizontal and the vertical velocity components on x are plotted in Fig. 5 for sample parameters of the wind flow, when the injection velocity largely exceeds the ambient flow velocity. It is clearly seen that a particle is adapted to the airflow over a distance of about $2U_i\tau$. For the selected parameters, this distance was 25 mm. Because the nozzle of the injection device was

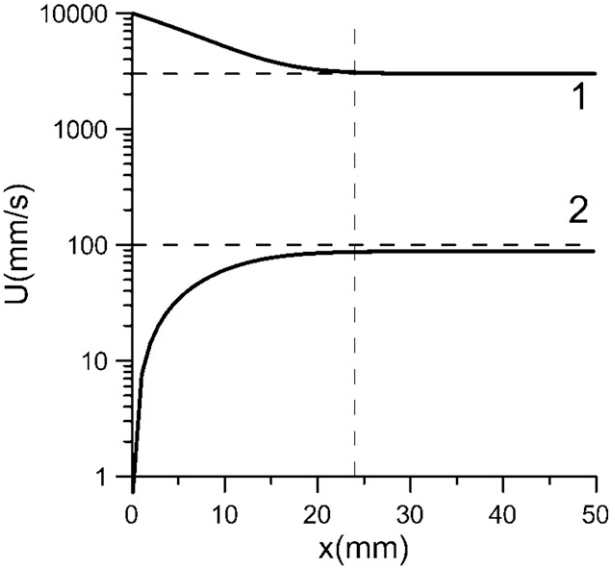

FIG. 5. Adaptation of a particle injected in the airflow. Horizontal (one solid curve) and vertical (two solid curves) velocities of a particle via downstream coordinate for sample parameters: flow velocity $U_{f||} = 3$ m s^{-1} and $U_{f\perp|} = 0.1$ m s^{-1}; injection velocity $U_{i||} = 10$ m s^{-1}; and $\tau = 1.2 \times 10^{-3}$ s. Dashed curves are for flow velocities.

positioned at the distance of 35 cm from the working window, we can conclude that the particle velocity was adapted to the airflow. This conclusion is confirmed by direct measurements of the average airflow velocity by the Pitot tube and root-mean-square of the horizontal velocity fluctuations by hot-wire probe, which show no effect of the compressed pressure injection at the distance of 35 cm from the nozzle of the injection device.

A 532-nm continuous Laser Complete System (LCS) 318–500-mW Nd:Yag laser beam transformed into a light sheet through a series of lenses was used to illuminate the area under investigation. The laser sheet about 3 mm thick was located in the middle of the tank. A CCD high-speed camera recorded images of the lightened particles in the turbulent airflow with the rate of 1000 frames per second (i.e., $t_{\text{exp}} = 0.5$ ms; Figs. 1, 3). The dimensions of the visualized area were 500×1280 pixels (107×274 mm^2).

It should be mentioned that the particle motion in the airflow is three dimensional (3D), so, for obtaining correct 2D velocity fields, the typical transversal displacement of particles during the exposition time should be less than the laser sheet thickness l_n,

$$v' t_{\text{exp}} \ll l_n, \tag{2.6}$$

where v' is a typical transversal velocity and t_{exp} is the exposition time of the CCD camera. Under this condition, only a small fracture of the total amount of particles seeding the working area will leave it or come to the adjacent frames. In the current experiments, $l_n = 3$ mm; $t_{\text{exp}} = 0.5$ ms; and $v' \sim u^*$, where u^* is friction velocity, the maximum value of u^* in this experiment was about 200 mm s^{-1} (see Table 2), and then $v' t_{\text{exp}} \sim 0.1$ mm (i.e., the sheet thickness is about an order of magnitude greater than the transversal particle displacement during the exposition time). Therefore, the transversal particle motion has an insignificant impact on correct estimation of the 2D velocity field by the PIV algorithm.

Each experiment was repeated 30 times to provide an ensemble for averaging. The duration of each run varied from 200 to 600 ms (limited by the duration of particle injection).

c. *Initial processing of the images*

Digital image processing included several stages. In the beginning, the wave profile was determined for each frame. It was visualized as a bright continuous contour because of the illuminated particles seeded at the water surface. In this experiment, the contrast of the air–water interface sufficient for automatic processing was not achieved for each frame. The wave profiles with poor contrast were processed manually (marked and then interpolated). For reducing the manual work, the same interpolated contour shifted according to celerity was used for consequent frames where the wave profiles were close to the initial one interpolated manually. For the waves with the period 0.4 s in this experiment, the same contour can be used for 30 frames (0.03 s) close to the wave trough. The wave profile changed faster near the wave crest; hence, the same contour was used only for 10 frames (0.01 s). The coordinate grid of interrogation windows for obtaining velocity field was configured according to the curvilinear water surface for each frame (Fig. 6).

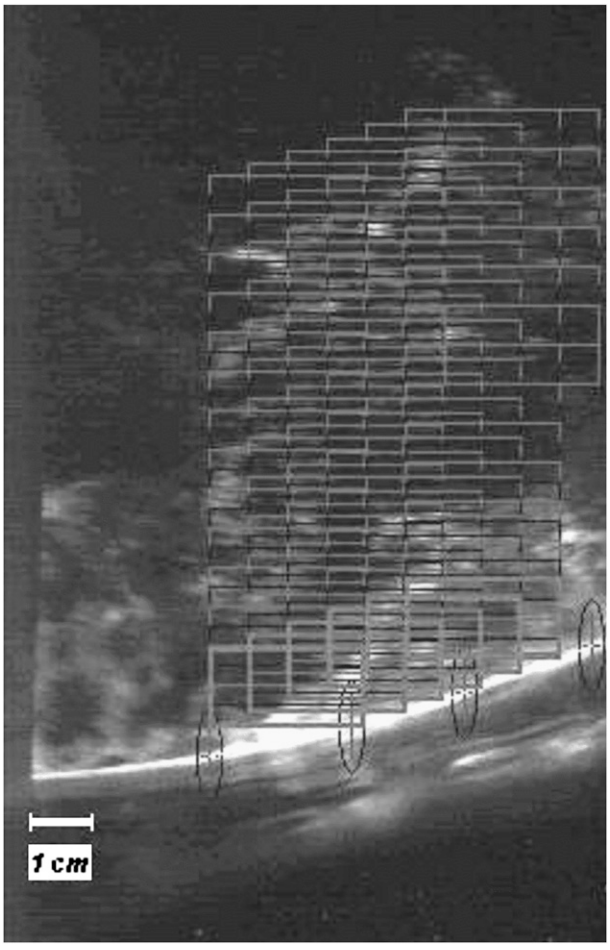

FIG. 6. Illustration of locations of the interrogation windows above the curvilinear water surface.

On the examples of the frames (Fig. 14), it is seen that some areas in the images do not contain particles because of the inhomogeneous seeding. So, before applying the PIV algorithm, the images were automatically processed for selecting interrogation windows where the illuminated particles were present. For this purpose, the image intensity gradient averaged over each ith interrogation window,

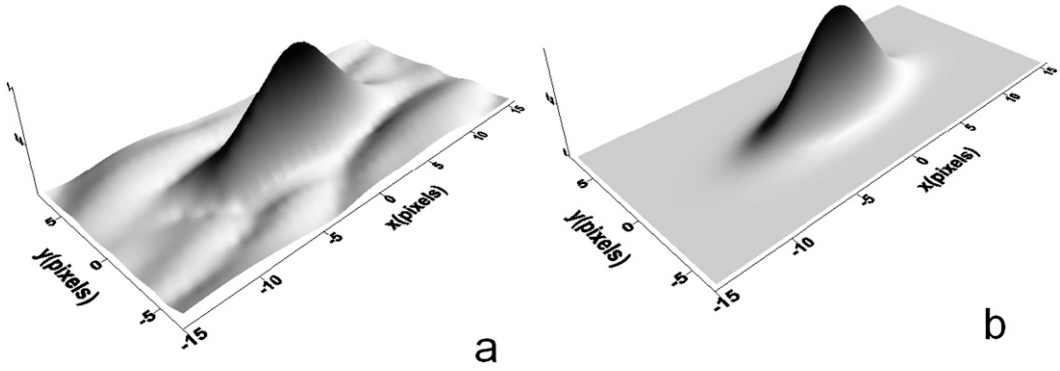

FIG. 7. (a) Typical example of CCF of subsequent images in these experiments and (b) approximation of the CCF from previous images by the expression in Eq. (2.8).

$$g_i = \sqrt{\frac{1}{mn}\sum_{k,j}^{m,n}\left[\left(\frac{\partial I}{\partial x_k}\right)^2 + \left(\frac{\partial I}{\partial y_j}\right)^2\right]}$$

(where $m = 32$ and $n = 16$ are the numbers of pixels in the interrogation window) was calculated and compared with the image intensity gradient averaged over the entire working area,

$$G = \sqrt{\frac{1}{MN}\sum_{k,j}^{M,N}\left[\left(\frac{\partial I}{\partial x_k}\right)^2 + \left(\frac{\partial I}{\partial y_j}\right)^2\right]},$$

where $M = 500$ and $N = 1280$ are the numbers of pixels in the entire working window. In the absence of particles, the image intensity gradient in the interrogation window was close to zero; the presence of particles increased the gradient dramatically. The interrogation windows that did not fit the gradient criterion $g_i/G > a$ were excluded from processing. The threshold coefficient $a = 6$ corresponded to the presence in the interrogation window of 7–8 images of particles with sufficient contrast for automatic processing.

d. Modified iterative multigrid PIV method

After eliminating ''empty'' interrogation windows, the velocity field was retrieved by means of a modified iterative multigrid cross-correlation PIV algorithm proposed in the paper by Scarano and Riethmuller (1999). The sizes of the interrogation window for the first approximation in data processing were 32 pixels in the vertical direction and 64 pixels in the horizontal direction. Then, the resolution was refined to 16×32 pixels with the final resolution being 3.4 mm in the vertical direction and 6.8 mm in the horizontal direction.

The modification of the algorithm suggested by Scarano and Riethmuller (1999) concerned the procedure of subpixel approximation for the cross-correlation function (CCF) of two subsequent images. In the classical PIV scheme based on extremely short exposure time and ''frozen'' images of illuminated particles, CCF is close to the isotropic two-dimensional Gauss peak function (see, e.g., Adrian 1991; Fincham and Spedding 1997; Bolinder 1999),

$$f(x,y) = \exp\left[-\frac{(x-x_0)^2 + (y-y_0)^2}{\delta^2}\right], \qquad (2.7)$$

where x_0 and y_0 are the coordinates of maxima and δ is half width.

In our experiments with low intensity continuous laser illumination, the exposure time (0.5 ms) was only 2 times less than the separation time between the frames; therefore, the strip-like images of the particles tracks were acquired with the maximum length of the track of about 7 pixels. As a result, CCD of two subsequent images was anisotropic with oblique main axis (see Figs. 7a,b).

We proposed a modified surface for CCF approximation,

$$f(x,y) = \exp\left[-\frac{(x-x_0)^2}{\delta_x^2} - \frac{(y-y_0)^2}{\delta_y^2} - \frac{(x-x_0)(y-y_0)}{\delta_{xy}}\right], \qquad (2.8)$$

where δ_x and δ_y are half widths of the CCF peak in the x and y directions, respectively, and δ_{xy} is the coefficient determined by the inclination of the tracks. An example of the best fit of the experimental data by the function in Eq. (2.8) is shown in Figs. 7c,d.

Errors in retrieving (x_0, y_0) from the subpixel interpolation in Eq. (2.8) were estimated by a numerical experiment usually conducted for testing accuracy of PIV algorithms (see, e.g., Fincham and Spedding 1997; Bolinder 1999). Typical experimental images were artificially shifted by a definite distance by means of subpixel

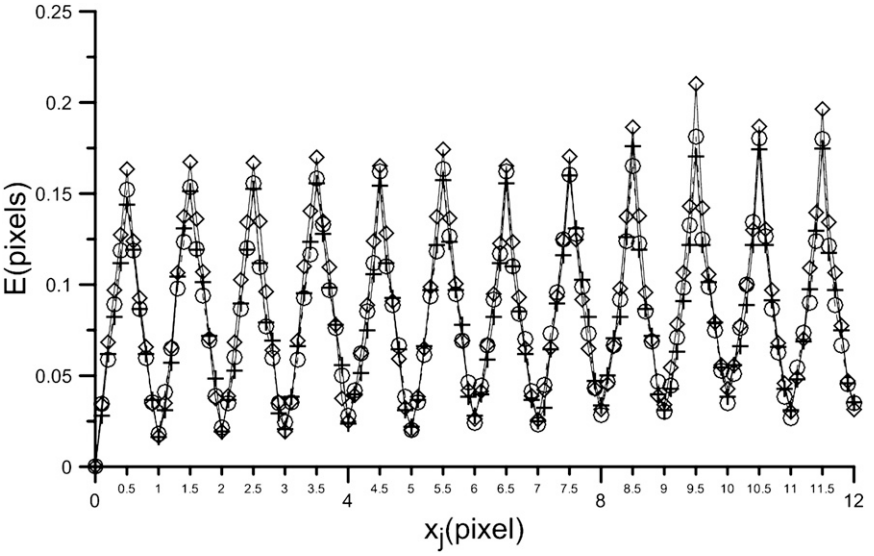

FIG. 8. Root-mean-square error of a particle displacement vs horizontal displacement x_j, for the three values of vertical displacement: 0.1 (crosses), 0.5 (diamonds), and 1 pixel (circles).

interpolation by a bicubic spline. Fragments of images for test processing were taken at different heights from the water surface, which corresponded to different track lengths. The test images were processed for the full range of displacements in the horizontal direction from 0 to 12 pixels with a step of 0.1 pixel and for three different vertical displacements: 0.1, 0.5, and 1 pixel. For each value of displacement, the fragment of the image containing 512 of 32 × 16 pixel interrogation windows with 50% overlap was processed by the modified iterative multigrid PIV algorithm and the root-mean-square error in the displacement was calculated,

$$E_{\text{rms}} = \sqrt{\frac{1}{N}\sum_{i=1}^{N}(r_{mi} - r_{\text{true}})^2},$$

where r_m is the measured displacement for the ith interrogation window, r_{true} is the actual displacement, and $N = 512$.

In Fig. 8, E_{rms} is plotted versus displacement. Similar dependences were obtained by Fincham and Spedding (1997) and Bolinder (1999) for the case of the iterative multigrid method with subpixel extrapolation. Obviously, the minimum errors correspond to the displacements by an integer numbers of pixels, and the maximum errors occur for integer and half-pixel displacements. Slight monotonous increasing of the error with increasing displacement is also visible in Fig. 8. A similar trend was observed by Bolinder (1999) for isotropic CCF. The maximum value of error was 0.22 pixels for the horizontal direction and 0.13 pixels for the vertical direction. For our experiments, this corresponds to the velocity magnitudes of 5 and 3.5 cm s^{-1}, respectively. These estimations can be taken as the upper estimate of error for the mean velocity retrieved by the iterative multigrid PIV method with anisotropic CCF in our experiments.

3. Statistical data processing and presentation

a. Statistical ensemble of water elevation and velocity field

The specific feature of the used high-speed camera, which prescribed the algorithm of data processing, is a narrow working window covering only a small part of the wavelength. The simplest approach to data processing for this experimental setup is analysis of time dependences of the measured quantities at fixed horizontal coordinate x_{0i}. The obtained time series are similar to the data measured by contact point sensors (see, e.g., Hsu et al. 1981; Hsu and Hsu 1983), but implementation of a noninvasive measuring method based on fast video filming gives advantages of dramatic decreasing of flow disturbances and high space resolution in the vertical direction, which cannot be achieved by contact sensors. The time series of the two velocity components at fixed distances from the water surface, as well as the water elevation and slope, were obtained for each experimental run at definite x_{0i}. The velocity components were retrieved from video films by the PIV technique, the water elevation was obtained from contrast analysis of the frames, and the slope was calculated as a numerical derivative of the water elevation with

respect to the horizontal coordinate. Those quantities were measured at four x coordinate points spaced apart by 15 mm in the central part of the working area; thus, they corresponded to different interrogation windows. Then, about 120 time series from 200 to 400 ms were obtained for each experiment to form statistical ensembles.

The procedure of conditional (on the phase of water elevation) averaging, or ''phase averaging,'' was then applied for all the recorded time series. It is frequently used in data processing in the experiments on wind interaction with paddle-generated waves (see, e.g., Hsu et al. 1981; Papadimitrakis et al. 1984). The use of the Fourier decomposition generalizes this technique to the case of broadband signals as is described, for example, in the papers by Donelan et al. (2006). The phase averaging is equivalent to the statistical averaging, if the scales of turbulent fluctuations are less than the wavelength.

As a result of the ensemble (conditional on the phase of water elevation) averaging, the mean velocity vector field is obtained as a function of time on one wave period and vertical coordinate. It can be represented as two-dimensional fields in the plane (y, t). In the case of a progressive water wave with celerity c, the airflow fields averaged over turbulent fluctuations depend on x and t as $q(x - ct, y)$. Then, the dependence of q on x can be easily obtained from the dependence on t. This way of data presentation is used below.

The averaged airflow fields were calculated according to definition of the ensemble (conditional on the phase of water elevation) average. The mean velocity vector is written as

$$\langle \mathbf{u} \rangle (y_j, t_i) = \frac{1}{n_{ij}} \sum_{k=1}^{n_{ij} > N_{\text{avg}}} \mathbf{u}_k (y_j, t_i + t_{0k}). \tag{3.1}$$

The normal $\langle u'^2 \rangle$ and $\langle w'^2 \rangle$ and tangential $\langle u'w' \rangle$ turbulent stresses have the form

$$\langle u'^2 \rangle (y_j, t_i) = \frac{1}{n_{ij}} \sum_{k=1}^{n_{ij}} [u_k (y_j, t_i + t_{0k}) - \langle u \rangle (y_j, t_i)]^2, \tag{3.2}$$

$$\langle w'^2 \rangle (y_j, t_i) = \frac{1}{n_{ij}} \sum_{k=1}^{n_{ij}} [w_k (y_j, t_i + t_{0k}) - \langle w \rangle (y_j, t_i)]^2, \quad \text{and} \tag{3.3}$$

$$\langle u'w' \rangle (y_j, t_i) = \frac{1}{n_{ij}} \sum_{k=1}^{n_{ij}} [u_k (y_j, t_i + t_{0k}) - \langle u \rangle (y_j, t_i)] \times [w_k (y_j, t_i + t_{0k}) - \langle w \rangle (y_j, t_i)], \tag{3.4}$$

where t_{0k} is the time reference point corresponding to the crest of the surface wave in each kth series, n_{ij} is the number of the acquired data points in a given interrogation window fitting the gradient validity criteria (see section 2c) at the level y_j and time t_i counted from the reference point t_{0k}, and $\langle u \rangle$ and $\langle w \rangle$ are the ensemble-averaged wind velocity components.

b. Curvilinear coordinates and governing equations

The vertical scale of the wind velocity profile (the scale of the viscous sublayer, typically equal to $20 - 30\nu_a/u_*$) near the water surface is smaller than the wave amplitude. Therefore, the wind velocity profile is usually represented in the curvilinear coordinates, which follow the shape of the wavy boundary (Miles 1959; Benjamin 1959; Gent and Taylor 1976; Hsu et al. 1981; Al-Zanaidi and Hui 1984). The most convenient way for data representation is the curvilinear wave-following coordinate transformation such as, for example, proposed by Hsu et al. (1981),

$$\begin{aligned} x &= x^*, \\ y &= y^* + f(y^*)\tilde{\eta}(x^*, t), \end{aligned} \tag{3.5}$$

where $\tilde{\eta}(x^*, t)$ is the shape of the surface elevation and $f(y^*)$ is a function equal to 1 at $y^* = 0$. For instance, Hsu et al. (1981) exploited $f(y^*)$ decreasing to zero at the upper boundary of the airflow H. For a harmonic surface elevation,

$$\tilde{\eta}(x^*, t) = a \cos(\omega t - kx^*), \tag{3.6}$$

it was the following

$$f(y^*) = \frac{\sinh k(y^* + H)}{\sinh kH}. \tag{3.7}$$

In that paper, the simplest expression for the function $f(y^*)$ was used: namely, $f(y^*) = 1$; then,

$$\begin{aligned} y^* &= y - \eta(x, t), \\ x^* &= x, \quad \text{and} \\ t^* &= t, \end{aligned} \tag{3.8}$$

where $\eta(x, t)$ is the surface elevation. The governing equations for the airflow in the coordinates in Eq. (3.8) are written in the following forms (see Hsu et al. 1981):

x momentum equation,

$$\frac{\partial \langle u \rangle}{\partial t^*} - \frac{\partial \langle u \rangle}{\partial y^*}\frac{\partial \eta}{\partial t^*} + \langle u \rangle \left(\frac{\partial \langle u \rangle}{\partial x^*} - \frac{\partial \langle u \rangle}{\partial y^*}\frac{\partial \eta}{\partial x^*} \right) + \langle v \rangle \frac{\partial \langle u \rangle}{\partial y^*} + \frac{\partial \langle p \rangle}{\partial x^*} - \frac{\partial \langle p \rangle}{\partial y^*}\frac{\partial \eta}{\partial x^*} = \frac{\partial \sigma_{11}}{\partial x^*} - \frac{\partial \sigma_{11}}{\partial y^*}\frac{\partial \eta}{\partial x^*} + \frac{\partial \sigma_{12}}{\partial y^*}; \tag{3.9}$$

y momentum equation,

$$\frac{\partial\langle v\rangle}{\partial t^*} - \frac{\partial\langle v\rangle}{\partial y^*}\frac{\partial\eta}{\partial t^*} + \langle u\rangle\left(\frac{\partial\langle v\rangle}{\partial x^*} - \frac{\partial\langle v\rangle}{\partial y^*}\frac{\partial\eta}{\partial x^*}\right) + \langle v\rangle\frac{\partial\langle v\rangle}{\partial y^*} + \frac{\partial\langle p\rangle}{\partial y^*} = \frac{\partial\sigma_{12}}{\partial x^*} - \frac{\partial\sigma_{12}}{\partial y^*}\frac{\partial\eta}{\partial x^*} + \frac{\partial\sigma_{22}}{\partial y^*}; \quad \text{and} \quad (3.10)$$

continuity equation,

$$\frac{\partial\langle u\rangle}{\partial x^*} - \frac{\partial\langle u\rangle}{\partial y^*}\frac{\partial\eta}{\partial x^*} + \frac{\partial\langle v\rangle}{\partial y^*} = 0, \quad (3.11)$$

where $\langle u\rangle$ and $\langle v\rangle$ are the x and y velocity components averaged over turbulent fluctuations, $\langle p\rangle$ and $\sigma_{ij} = \langle u_i' u_j'\rangle$ are the normalized pressure and turbulent stresses. Here, the average viscous stresses are included into σ_{ij}, and then the eddy viscosity coefficient is a sum of turbulent and molecular viscosity coefficients. The kinematic boundary condition at the water surface reads as

$$\left(\langle v\rangle - \langle u\rangle\frac{\partial\eta}{\partial x^*} - \frac{\partial\eta}{\partial t^*}\right)\Bigg|_{y^*=0} = 0. \quad (3.12)$$

The ensemble-averaged fields can be decomposed into the mean fields and wave disturbances induced in the airflow by the wave at the water surface $q_{\sim}$; then we have

$$\langle q\rangle = Q(y^*) + q_{\sim}(x^*, y^*, t^*).$$

It should be emphasized that here we consider the ensemble averaging of aerodynamic fields over turbulent fluctuations, whereas the water elevation is treated as a deterministic function of time and coordinates, even if it is a complicated function of x^* and t^*, which can be decomposed into a sum of the Fourier harmonics. The field of water elevation gives rise to the ensemble-averaged disturbances in the turbulent airflow over waves, $q_{\sim}(x^*, y^*, t^*)$. In the case of wind over the paddle-generated harmonic waves studied here, there were wind ripples excited at the water surface in addition to the dominant wave. These disturbances contribute to the water elevation and induce disturbances of the corresponding scale in the airflow.

In the theoretical model presented in section 6, we suggest that each harmonic surface wave induces the corresponding disturbances in the airflow, regardless of other harmonic disturbances; that is, we consider the wave disturbances in the air within the linear approximation applicable for the case of small Reynolds numbers (see Batchelor 1967). In the turbulent regime of the flow, the Reynolds number as defined by the molecular kinematic viscosity is huge, but the average flow dynamics described within the Reynolds equations [Eqs. (3.9) and (3.10)] is determined by the effective Reynolds number, which is defined by the eddy viscosity coefficient. The effective Reynolds number for the wave disturbances induced in the airflow is $\mathrm{Re}_{\mathrm{eff}} = (u_{\sim}\delta_{\sim}/\nu_{\mathrm{turb}})k\delta_{\sim}$, where $u_{\sim} = kac, \delta_{\sim} = \kappa u_*/kc$ (the estimates for the scale of the wave-induced disturbances are presented in section 5), $\delta_{\sim}$ are the scales of the wave disturbance (c is phase velocity and ka is steepness), $\nu_{\mathrm{turb}} = \kappa u_*\delta_{\sim}$ is the effective value of the eddy viscosity coefficient for this wave disturbance, and then $\mathrm{Re}_{\mathrm{eff}} = ka$. In this experiment, $ka = 0.15$–0.3 and $\mathrm{Re}_{\mathrm{eff}} < 1$, so one can expect that the low effective Reynolds number approximation is applicable.

In the zero-order approximation with respect the wave disturbances, the y momentum equation yields the following expression for the mean fields:

$$\frac{\partial P}{\partial y^*} = \frac{\partial\Sigma_{22}}{\partial y^*}. \quad (3.13)$$

Here, P is mean pressure and Σ_{22} is mean turbulent normal stress.

In the low effective Reynolds number approximation, the wave-induced disturbances are described within the linearized governing equations, which in the coordinates in Eq. (3.8) are as follows:

x momentum equation,

$$(U-c)\left(\frac{\partial u_{\sim}}{\partial x^*} - \frac{\partial\eta}{\partial x^*}\frac{dU}{dy^*}\right) + v_{\sim}\frac{dU}{dy^*} + \frac{\partial p_{\sim}}{\partial x^*} - \frac{\partial P}{\partial y^*}\frac{\partial\eta}{\partial x} = \frac{\partial\sigma_{11\sim}}{\partial x^*} + \frac{\partial\sigma_{12\sim}}{\partial y^*} - \frac{\partial\Sigma_{11}}{\partial y^*}\frac{\partial\eta}{\partial x}; \quad (3.14)$$

y momentum equation,

$$(U-c)\frac{\partial v_{\sim}}{\partial x^*} + \frac{\partial p_{\sim}}{\partial y^*} = \frac{\partial\sigma_{12\sim}}{\partial x^*} + \frac{\partial\sigma_{22\sim}}{\partial y^*} - \frac{\partial\Sigma_{12}}{\partial y^*}\frac{\partial\eta}{\partial x}; \quad \text{and} \quad (3.15)$$

continuity equation,

$$\frac{\partial u_{\sim}}{\partial x^*} - \frac{\partial\eta}{\partial x^*}\frac{dU}{dy^*} + \frac{\partial v_{\sim}}{\partial y^*} = 0, \quad (3.16)$$

where Σ_{ij} are the mean turbulent stresses and $\sigma_{ij\sim}$ are wave disturbances of the turbulent stresses.

We notice here that the system of equations [Eqs. (3.9)–(3.16)] is not closed, because the number of unknown functions exceeds the number of equations. Here, no closing hypothesis was used; instead, the turbulent stresses were retrieved from the experimental data by means of ensemble averaging.

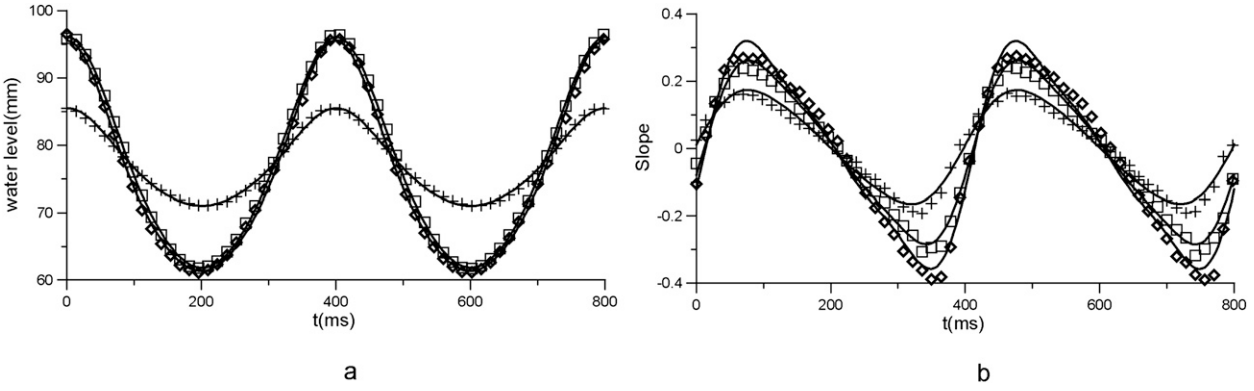

FIG. 9. Average (a) water elevation and (b) slope retrieved from the fast video [for the wavemaker amplitudes 6.5 (crosses), 14 (diamonds), and 20 mm (squares)]. Solid curves are approximation by Eq. (4.1).

4. Ensemble-averaged fields: Water elevation

The major purpose of this study is investigation of a turbulent airflow over the wavy water surface and comparison of the experimental results with the theoretical predictions (Reutov and Troitskaya 1995). Within the adopted model, the surface wave field determines boundary conditions for the airflow. We expected that parameters of surface waves in the experiment would be substantially different from the predictions of the theory of potential surface gravity–capillary waves in deep waters. To avoid the errors, the wave parameters were measured in experiments. In this section, parameters of the water waves obtained from the statistical processing of digital video are described.

The time series of water surface elevation and slopes were retrieved from the fast video using the procedure described in section 2c. The initial phase shift of the wave was retrieved from the least squares fitting of the profile of water elevation by the Stokes equation [Eq. (4.1)] in each experimental run. Then, the records were phase matched and averaged over the statistical ensemble; the results are plotted in Fig. 9. One can see in the figure that the measured water elevation fits the Stokes formula very well, in spite of the presence of wind flow. At the same time, deviations of the water slope from the Stokes formula are more pronounced, probably because of errors of numerical calculation of derivatives,

$$\xi = z_0 + A[\cos(2\pi Ft) + S/2\cos(4\pi Ft) + 3/8S^2\cos(6\pi Ft)],$$
$$\xi_x = -S\sin(2\pi Ft) - S^2\sin(4\pi Ft) - 9/8S^3\sin(6\pi Ft). \quad (4.1)$$

Fitting of the experimental data by the expressions in Eq. (4.1) allows finding A and S independently from the first and second equations, respectively.

The wave amplitudes and maximum slopes versus the wavemaker amplitude are presented in Fig. 10. The curves are not linear; the tendency to saturation is clearly visible in the amplitude dependence (Fig. 10a); and, surprisingly, at large amplitudes increasing of the amplitude of the paddle oscillations was accompanied with decreasing of the maximum slope of the generated waves (Fig. 10b). It should be taken into account that, for the cases of two largest amplitudes (14 and 20 mm), wave breaking occurred, which is clearly visible in the video films and was also confirmed by the shape of the frequency spectrum of short surface waves, where the spectral amplitude of the high frequency part of the spectra was enhanced substantially (see Fig. 2b).

Because the wave amplitude A and magnitude of the slope S were measured independently, it was possible to estimate the wavenumber of the paddle-generated wave in this experiment, $k = S/A$; because the frequency f of the wave is specified by the wavemaker, the phase speed can be calculated directly, $c = 2\pi f/k$. The wavenumber and phase velocity of the wave as a function of the wave slope obtained in this way are plotted in Fig. 11. It is clearly seen that for a smooth wave the wavelength and phase velocity are close to the values predicted by the linear potential theory of water waves of given frequency, whereas for steep and especially breaking waves the wavelength (Fig. 11a) and phase speed (Fig. 11b) of the wave noticeably (up to 30%) exceeded the theoretical quantities. We supposed that this is related to the drift flow, which increased significantly in the presence of wave breaking due to transferring momentum to the mean flow by the breaking event (Phillips 1985; Phillips et al. 2001). To check this hypothesis, we estimated the drift flow in experiment. The flow velocity in the rectangle (80 × 300 pixels) below the wave trough was measured by means of the PIV algorithm applied to the particles seeding the water column and averaged

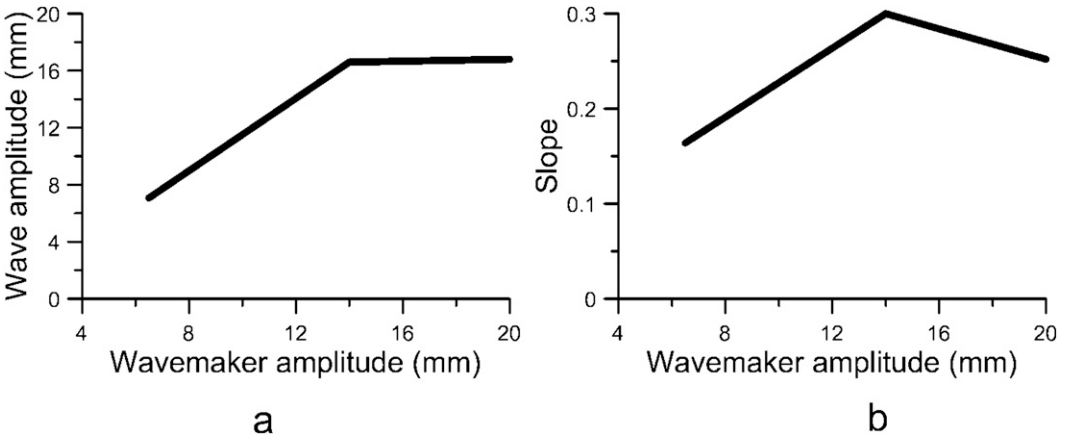

FIG. 10. The dependencies of (a) wave amplitude and (b) maximum slope vs the wavemaker amplitude.

over the wave period. The measured velocity essentially exceeded (see Fig. 12) the expected value of the Stokes drift estimated by the phase velocity of the wave in still water and the slope as follows: $v_{\text{drift}} = S^2 c$. The observed excess of the drift flow may be attributed to the action of the surface stress caused by the wind stress and wave breaking. A possible explanation of the wave slope decreasing in the presence of wave breaking is as follows. The wind stress and breaking wave transfer momentum to the mean flow and significantly enhance the drift flow. The drift flow increases the phase speed of the wave and, at a definite wave frequency, it increases the wavelength and decreases the wavenumber of the paddle-generated wave. In these experiments increasing of the wavelength was so great that it resulted in the decreased wave slope.

The measured parameters of the wave field for the wave frequency of 2.5 Hz and wind velocity of 4 m s^{-1} are listed in Table 1. They will be used in section 7 for comparison of the experimental data with the theoretical calculations.

5. Ensemble-averaged aerodynamic fields in air

a. Velocity and turbulent stresses

1) VELOCITY VECTOR FIELDS

Two components of the flow velocity were retrieved by means of the PIV algorithm and collected at the points with fixed horizontal coordinates. The obtained dependences of two components of the velocity field on time t and vertical coordinate y are presented as vector

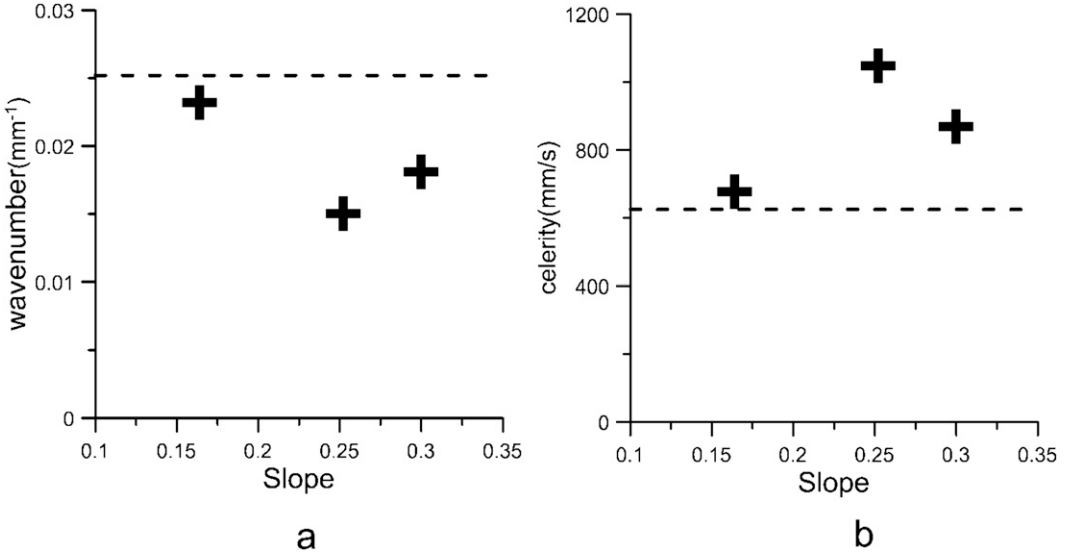

FIG. 11. (a) Wavenumber and (b) celerity vs maximum wave slope.

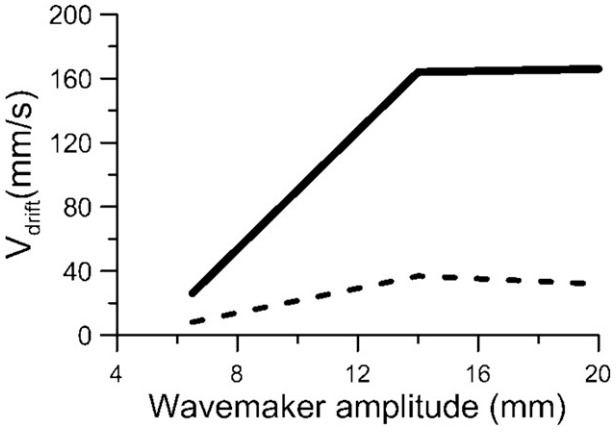

FIG. 12. Averaged over wave period, the flow velocity in the rectangle below the wave trough (solid curve) and the Stokes drift velocity (dashed curve).

maps. The positions of the vectors correspond to the centers of nonoverlapping interrogation windows and reflect the current space resolution of PIV processing. Examples of the maps retrieved from a single video film are presented in Fig. 13 in the wave-following reference frame in the plane ($x = \lambda - ct$, y), here λ is the wavelength retrieved from independent measurements of water elevation and slope for experiments 1 ($ka = 0.16$), 2 ($ka = 0.3$), and 3 ($ka = 0.25$). The effect of flow separation in the instant airflow velocity field can be identified in Figs. 14 b,d,f by typical patterns of the instant velocity vector maps in the wave-following reference frame. In the neighborhood of the wave crest in Figs. 14d,f, sharp decrease of the airflow velocity occurs at the lee side of the wave profile; it corresponds to a sharp peak in the vorticity field similar to that one observed by Reul et al. (1999, 2008) and Veron et al. (2007). Noticeable decrease of the airflow velocity is also visible in the lee of the smooth wave in Fig. 14b. A similar effect of flow separation near the crest of smooth waves was observed by Weissmann (1986) in smoke-based visualization. Complex structures (vortices, some sort of separation bubble) are visible in all vector maps. There are also convergence zones reflecting the three-dimensional character of a single flow field. The pictures are similar to the vector maps of the instant velocity field obtained by Reul et al. (1999, 2008) and Veron et al. (2007) by means of PIV processing of the instant velocity field.

Then, we averaged individual velocity vector fields obtained in all experimental runs corresponding to a definite set of parameters (see Table 1), conditionally sampled on the phase of the surface elevation. For this purpose, the velocity fields were matched to the phase of the water elevation and averaged over the ensemble

TABLE 1. Wave parameters.

No. of the run	1	2	3
Amplitude of the wavemaker oscillations (mm)	6.5	14	20
Wave amplitude (mm)	7.07	16.6	16.8
Wave slope	0.16	0.3	0.25
Wavenumber (mm^{-1})	0.023	0.018	0.015
Wavelength (mm)	271	348	419
Wave celerity (mm s^{-1})	677	869	1047

containing 100–120 time series. Because the flow series in different experimental runs are statistically independent, the conditional (on the wave phase) averaging is equivalent to statistical averaging or averaging over turbulent fluctuations. The conditionally averaged vector velocity fields in the airflow for experiments 1, 2, and 3 (see Table 1) are plotted in Fig. 15. As compared to the individual flow vector maps (Figs. 13a–c) the averaged velocity field appears to be smooth not only for the smooth wave (Fig. 15a) but also for the steep and breaking waves (Figs. 15b,c).

2) MEAN VELOCITY AND STRESS PROFILES

Averaging over a wave period yields profiles of mean velocity and stresses,

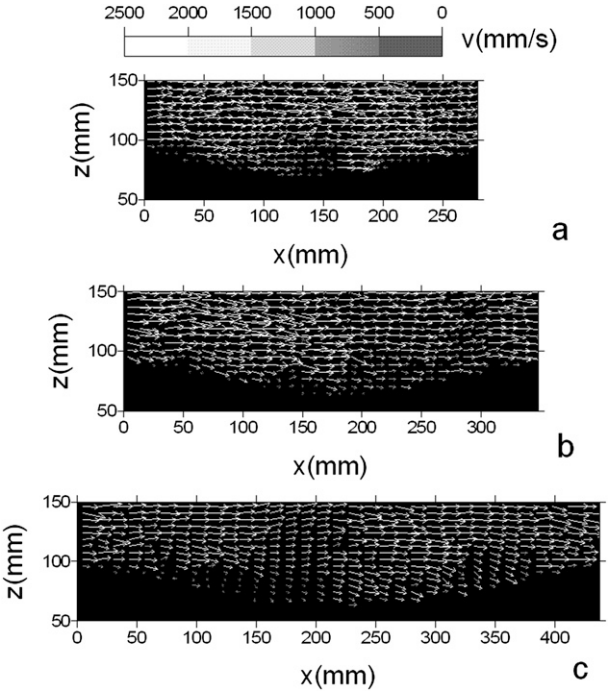

FIG. 13. A single realization of the vector velocity field in the wave-following reference frame: (a) experiment 1 ($ka = 0.16$), (b) experiment 2 ($ka = 0.3$), and (c) experiment 3 ($ka = 0.25$).

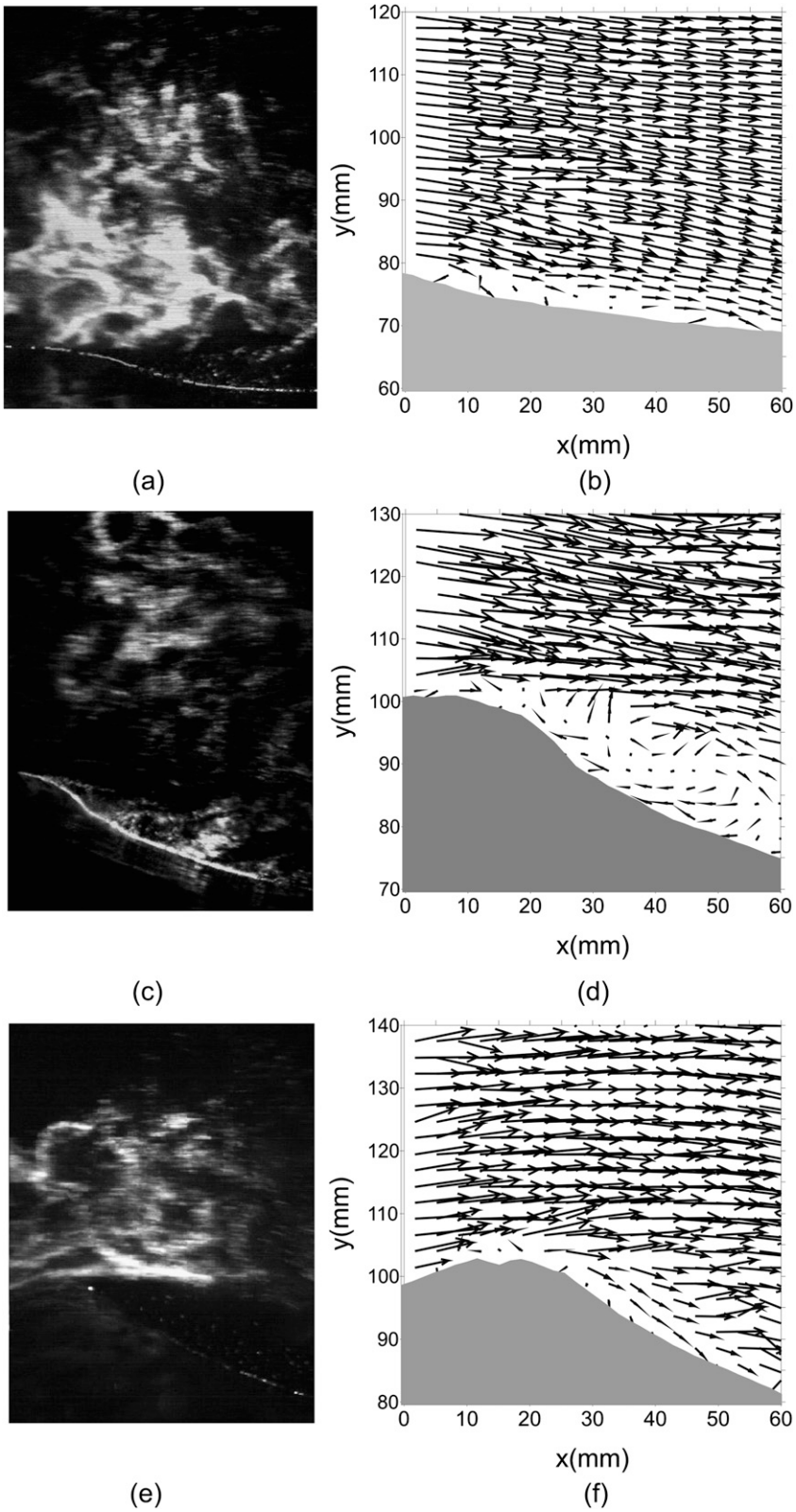

FIG. 14. Examples of the high-speed video frames for (a) experiment 1 ($ka = 0.16$), (c) experiment 2 ($ka = 0.3$), and (e) experiment 3 ($ka = 0.25$) and the corresponding airflow velocity vector maps for (b) experiment 1 ($ka = 0.16$), (d) experiment 2 ($ka = 0.3$), and (f) experiment 3 ($ka = 0.25$).

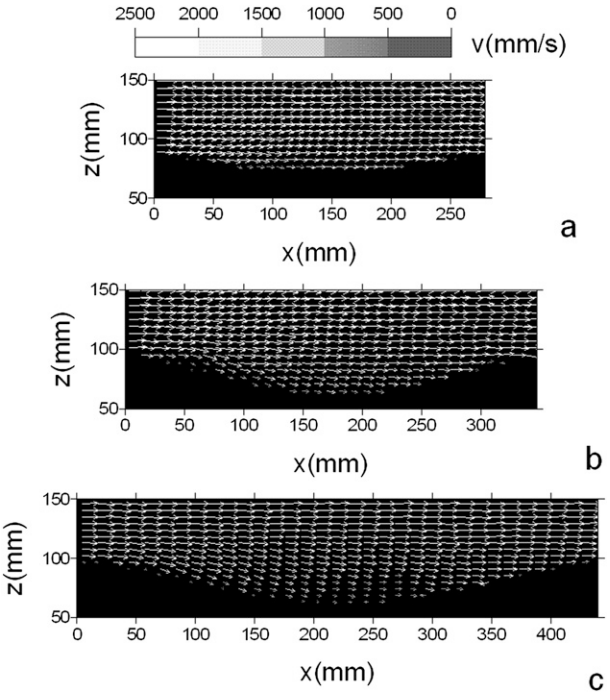

FIG. 15. Conditional (on the phase of the wave) averages of the vector velocity field in the airflow in the wave-following reference frame: (a) experiment 1 ($ka = 0.16$), (b) experiment 2 ($ka = 0.3$), and (c) experiment 3 ($ka = 0.25$).

$$U(y^*) = \frac{1}{N_i}\sum_{i=1}^{N_i}\langle u\rangle[y^* + \tilde{\eta}(t_i), t_i] \quad \text{and} \tag{5.1}$$

$$\Sigma_{ij}(y^*) = \frac{1}{N_i}\sum_{i=1}^{N_i}\langle u_i' u_j'\rangle[y^* + \tilde{\eta}(t_i), t_i]. \tag{5.2}$$

Here, N_i is the number of points involved in averaging at each level y^* over the curved surface.

The average velocity U profiles are presented in Fig. 16a for the first ($ka = 0.16$), second ($ka = 0.3$), and third ($ka = 0.25$) experiments in semilogarithmic coordinates. In these experiments, the working window was limited at the top by 70 mm because of the construction of the device for particle injection, so we did not observe the wake part of the turbulent boundary layer positioned at approximately 140 mm from the undisturbed water surface. For $y^* > 15$–20 mm, the mean velocity profiles are logarithmic. The straight lines in Fig. 16a represent the logarithmic approximation of the part of the flow for $y^* > 15$ mm,

$$U = \frac{u_*}{\kappa}\ln\frac{y^*}{z_0}. \tag{5.3}$$

The values of the wind friction velocity u_* retrieved from this expression are listed in Table 2. Deviations of the profile from the logarithmic function are clearly seen near the water surface. They indicate the region of action of the wave momentum flux and are more pronounced for large amplitudes of the waves in experiments 2 and 3. Also presented in Fig. 16a are the velocity profiles calculated for the case of the airflow over the smooth plane surface. Comparison with the measured profiles shows decreasing of the average velocity in the presence of waves at the water surface; that is, the effect of a supersmooth flow over the water surface unlike Hsu and Hsu (1983) was not observed.

The profiles of mean turbulent stresses Σ_{ij} are presented in Figs. 16b–d for experiments 1, 2, and 3. Within the logarithmic part of the turbulent boundary layer, the mean turbulent stresses tend to saturation with increasing distance from the surface, which is in agreement with the earlier experimental data (Hsu et al. 1981; Papadimitrakis et al. 1984). Similarly to the papers by Hsu et al. (1981) and Papadimitrakis et al. (1984), $\langle u'^2\rangle = \Sigma_{11}$ exceeds $\langle u'v'\rangle = \Sigma_{12}$ and $\langle v'^2\rangle = \Sigma_{22}$ by approximately an order of magnitude. The straight lines in Fig. 18b indicate the best fit of the constant part of the profile $\langle u'v'\rangle$. These values were used for alternative calculation of the wind friction velocity according to the following formula:

$$u_* = \sqrt{-\langle u'v'\rangle}. \tag{5.4}$$

The values of the wind friction velocity u_* are also presented in Table 2.

Following the method described in Melville et al. (2002), we investigated convergence of statistics of U and $\langle u'v'\rangle$ with the number of time series. The normalized errors in the statistical estimates of the magnitude of mean velocity δU_N and turbulent flux $\delta\langle u'v'\rangle_N$ were calculated as follows:

$$\delta U_N = \frac{1}{M}\sum_{i=1}^{M}\frac{|U_N(z_i) - U(z_i)|}{|U(z_i)|},$$

$$\delta\langle u'v'\rangle_N = \frac{1}{M}\sum_{i=1}^{M}\frac{|\langle u'v'\rangle_N(z_i) - \langle u'v'\rangle(z_i)|}{|\langle u'v'\rangle(z_i)|},$$

where $U(z)$ and $\langle u'v'\rangle(z)$ are the profiles of statistical estimates of horizontal velocity and turbulent momentum flux when referred to the entire number of time series (100–120, depending on the experiment) and $U_N(z)$ and $\langle u'v'\rangle_N(z)$ are the same values for N series. The sum is taken over M levels from minimum $z = 3.4$ mm to maximum $z = 72$ mm with the step 0.87 mm. Figures 16d,e shows that averaging over 100 series gives normalized error in the statistical estimate for velocity about

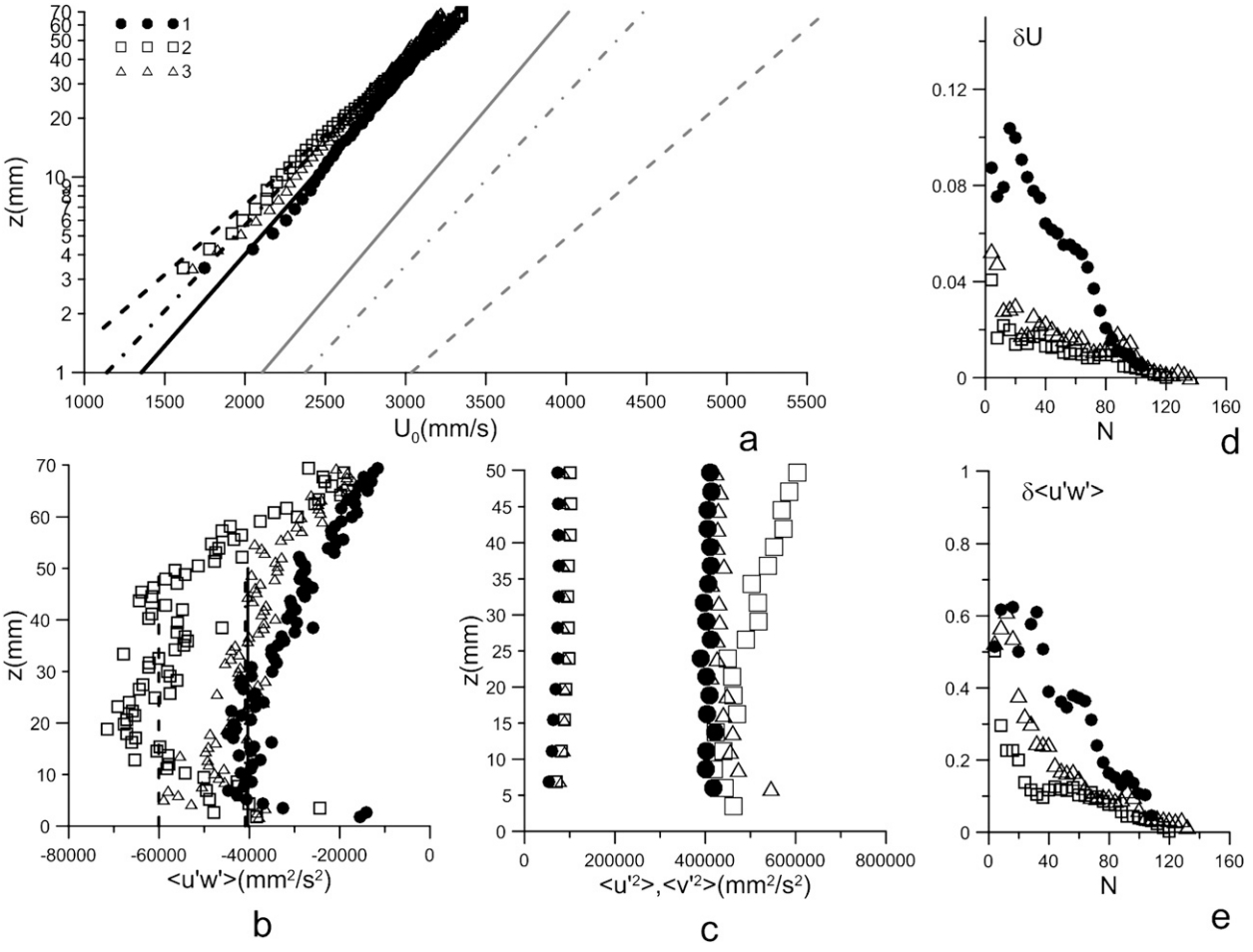

FIG. 16. Vertical profiles of (a) velocity and the following turbulent stresses: (b) $\langle u'v' \rangle$; (c) $\langle u'^2 \rangle$ and $\langle v'^2 \rangle$; and covariance of normalized errors (d) in velocity and (e) in turbulent stress for experiments 1 ($ka = 0.16$), 2 ($ka = 0.3$), and 3 ($ka = 0.25$).

1% and for turbulent momentum flux about 10% for experiments 2 and 3 ($ka = 0.3$ and 0.25) and about 15% for experiment 1 ($ka = 0.16$).

We also investigated the dependence of surface drag coefficient,

$$C_D = \frac{u_*^2}{U_0^2}, \tag{5.5}$$

for the fixed center line airflow velocity in the tank $U_0 = 4$ m s^{-1} on the parameters of the water waves. In Figs. 17a,b, C_D versus the wave amplitudes and slopes are plotted. The dependency of C_D on wave amplitude is nonmonotonous (Fig. 17a); it increases at small amplitudes and decreases when wave breaking occurs. Alternatively, C_D as a function of wave steepness is monotonously increasing (Fig. 17b). This suggests that surface roughness of the wavy water surface is determined by the effective steepness of the waves rather than by their amplitudes. This conclusion follows also from the theoretical model presented in section 6. It is clearly seen from the measurements of the water surface elevation (see section 4) that the wave breaking causes a decrease of the wave steepness (see Fig. 10b). Then it follows that, in the presence of wave breaking, the water surface resistance should decrease.

3) WAVE-INDUCED VELOCITY AND STRESS PROFILES IN THE AIRFLOW

The average velocity components at different levels conditionally sampled on the phase of the surface elevation (another representation of the velocity field in the airflow over waves) are plotted in Fig. 18 for the cases of smooth, steep, and breaking waves. They are represented as functions of time within 2 wave periods. For all cases the vertical velocity components close to the surface are approximately in phase with the water surface slope. The minimum of the horizontal velocity component is shifted to the leeward slope of the wave because of the sheltering effect.

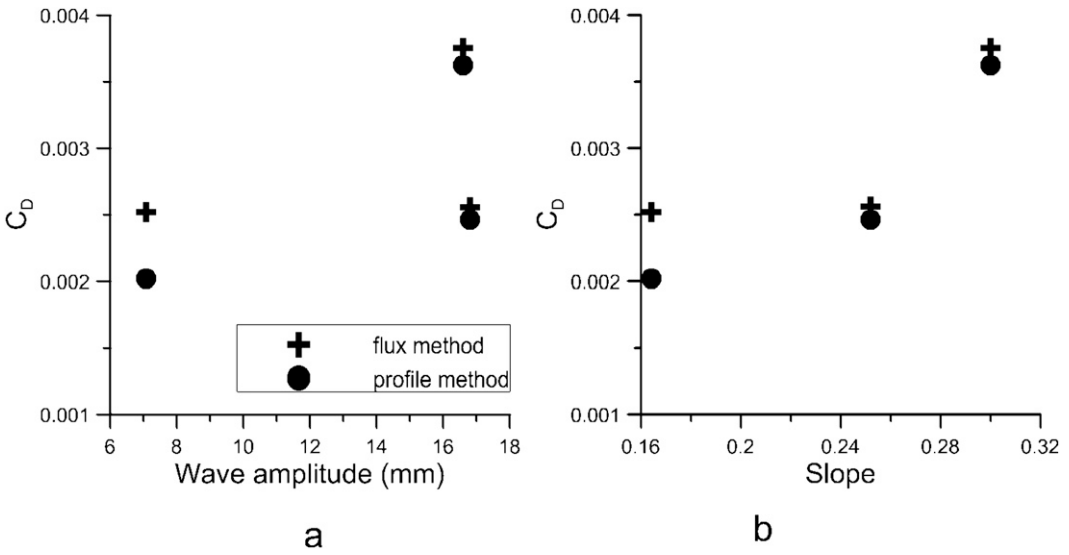

FIG. 17. The drag coefficient via wave (a) amplitude and (b) slope.

It obviously follows from Figs. 18a–e that the time dependence of the velocity components close to the water surface is noticeably inharmonic, especially in the case of steep waves; this indicates a substantial nonlinearity of the flow disturbances induced in the airflow by surface waves. Vertical profiles of the amplitudes of the harmonics in the Fourier series of disturbances of the horizontal and vertical velocity components,

$$u_1(y^*,t) = \frac{1}{2}\sum_{i=1}^{n} U_i(y^*)e^{2\pi ift} \quad \text{and} \tag{5.6}$$

$$v_1(y^*,t) = \frac{1}{2}\sum_{i=1}^{n} V_i(y^*)e^{2\pi ift}, \tag{5.7}$$

are plotted in Fig. 19. Obviously, for all experiments the amplitude of the first harmonic of wave-induced disturbances of horizontal velocity substantially exceeds the second and third ones. However, for the steep waves (experiment 2: $ka = 0.3$) and breaking waves (experiment 3: $ka = 0.25$), the amplitudes of the high harmonics of the horizontal velocity component are close to the main one near the water surface (Figs. 19b,c). This strong nonlinearity occurs only at the distance δ_{NL} of about 1 cm, which is much less than the vertical scale of the first harmonic k^{-1} and appreciably less than the peak-to-peak magnitude of the water elevation equal to approximately 33 mm (see Table 1). For the vertical velocity component, the main harmonics substantially exceed the high harmonics for all distances from the surface in all experiments (Figs. 19d–f).

The vertical profiles of the amplitudes of the harmonics in the Fourier series of disturbances of the tangential turbulent stress σ_{12} presented in Fig. 20 are written as

$$\sigma_{12}(y^*,t) = \frac{1}{2}\sum_{i=1}^{n} \Sigma_i(y^*)e^{2\pi ift}.$$

It is clear that for the smooth wave (experiment 1: $ka = 0.16$) the main harmonic of the wave-induced turbulent stress dominates the high ones, but for the steep waves (experiment 2: $ka = 0.3$) and breaking waves (experiment 3: $ka = 0.25$) the harmonics have close amplitudes; that is, the field of tangential stress disturbances induced in the airflow by water waves is strongly nonlinear.

We will also present in Fig. 21 the profiles of amplitudes and phase shifts of the first harmonic for two velocity components ($|u_1|$, φ_u) and ($|v_1|$, φ_v) and in Fig. 22 wave-induced turbulent stresses ($|r_{ij}|$, φ_{rij}), which are similar to the data presented in the papers by Hsu et al. (1981) and Papadimitrakis et al. (1984). The experimental errors are 15% for the magnitudes of the velocity components and about 20° for the phase. In this experiment $U_0/c = 4$–5.8; that is, the airflow velocity significantly exceeds the wave phase speed. Under these

TABLE 2. Mean wind flow integral parameters $U_0 = 4$ m s^{-1} and $f = 2.5$ Hz.

No. of the run	1	2	3
Amplitude of the wavemaker oscillations (mm)	6.5	14	20
Wind friction velocity (mm s^{-1}) by profile	180	240	200
Wind friction velocity (mm s^{-1}) by turbulent stress	200	245	200

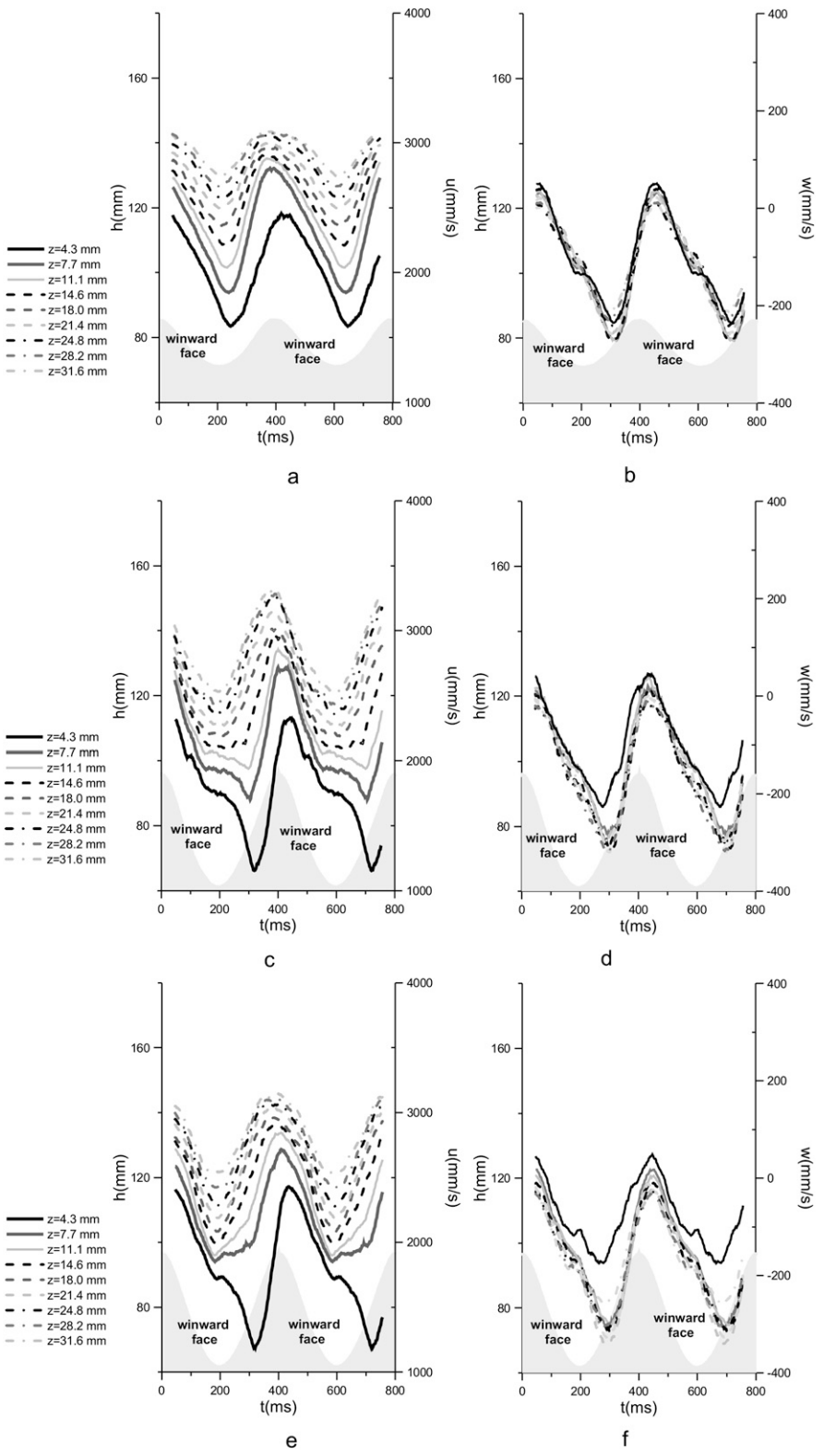

FIG. 18. Conditional (on the phase of the wave) averages of the surface elevation and (a),(c),(e) x and (b),(d),(f) y velocity components at different levels over the surface for experiments (a),(b) 1 ($ka = 0.16$), (c),(d) 2 ($ka = 0.3$), and (e),(f) 3 ($ka = 0.25$).

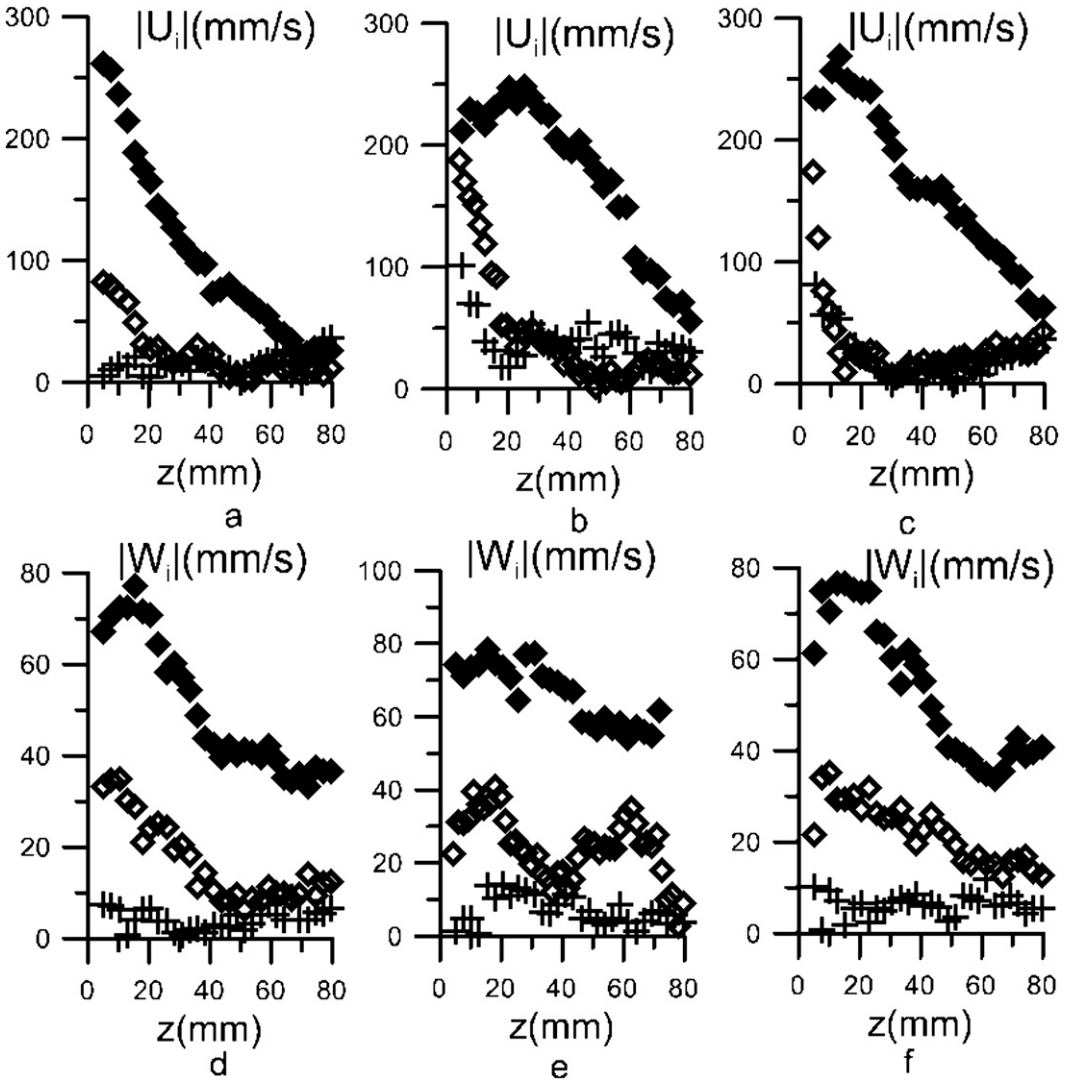

FIG. 19. Vertical profiles of magnitudes of the harmonics of (a)–(c) horizontal and (d)–(f) vertical velocities for experiments (a),(d) 1 ($ka = 0.16$); (b),(e) 2 ($ka = 0.3$); and (c),(f) 3 ($ka = 0.25$). Close diamonds show first harmonic, open diamonds show second harmonic, and crosses show third harmonic.

conditions, according to the potential theory of wave-induced disturbances in the airflow, the horizontal velocity is in phase with the water elevation, and the phase shift of the vertical velocity is 90°. The profiles in Figs. 21c,d are close to these predictions; the deviations arise from the impact of turbulent fluctuations and wind–wave interaction. In section 7, these measurements are compared with the results of calculation within the theoretical model that describes these effects quantitatively. It should be mentioned that the properties of the measured velocity profiles are similar to the analogous profiles considered in the paper by Papadimitrakis et al. (1984) for the case $U_0/c = 2.58$.

The profiles of magnitudes (±30%) and phases (±30°) of the first harmonic of the wave-induced turbulent stresses are plotted in Fig. 22. In section 5c, these functions (the profiles of the complex amplitudes of velocity components and stresses) are used for retrieving the wave-induced aerodynamic pressure from the measurements of the velocity field.

b. *The field of aerodynamic pressure in the airflow over waves*

One of the most important dynamic characteristics of the airflow over waves is distribution of air pressure at the wavy water surface, which determines the energy flux from wind to waves and their growth rate. By definition, the mechanical energy flux from the wind to a wave with frequency ω, wavenumber k, and amplitude a is

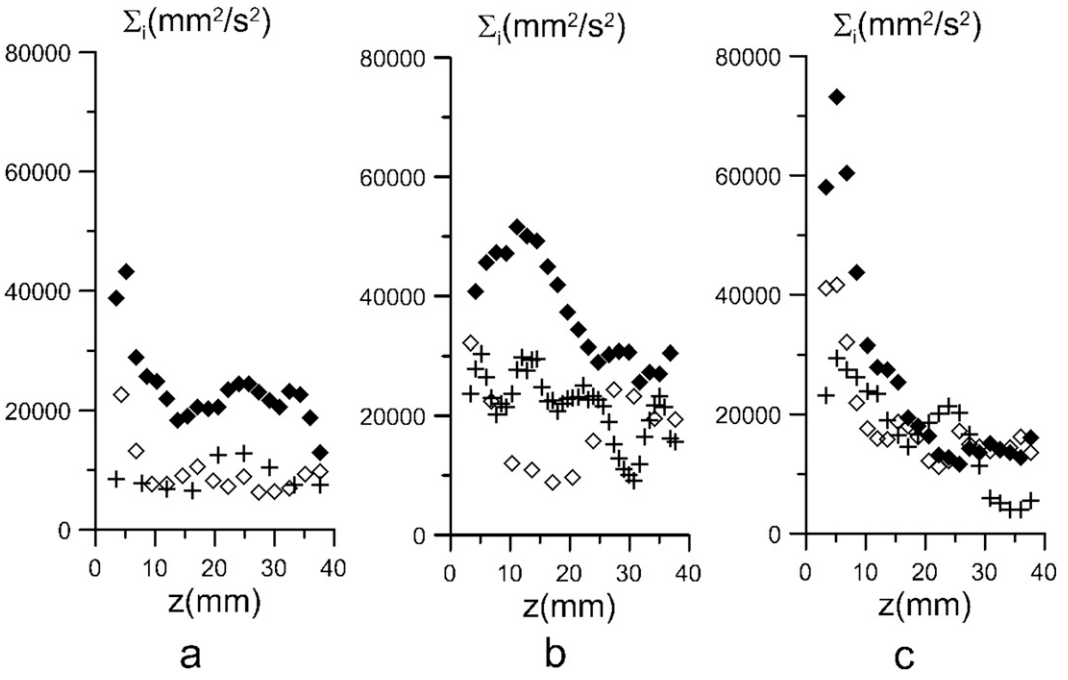

FIG. 20. Vertical profiles of the amplitudes of the harmonics in the Fourier series of wave-induced disturbances of the tangential turbulent stress σ_{12}: first harmonic (closed diamonds), second harmonic (open diamonds), and third harmonic (crosses).

$$\Pi = -\rho_a \langle (P_a - \sigma_{22})v - \sigma_{12}u \rangle, \tag{5.8}$$

where $P_a = p/\rho_a$ is the normalized pressure and $z\sigma_{ij}$ are the normalized turbulent stresses at the water surface S. In the wave-following curvilinear coordinates (x^*, y^*), the surface S is given by $y^* = 0$. The wave growth rate can be found from the energy balance equation,

$$\frac{dE}{dt} = \Pi|_{y^*=0}, \tag{5.9}$$

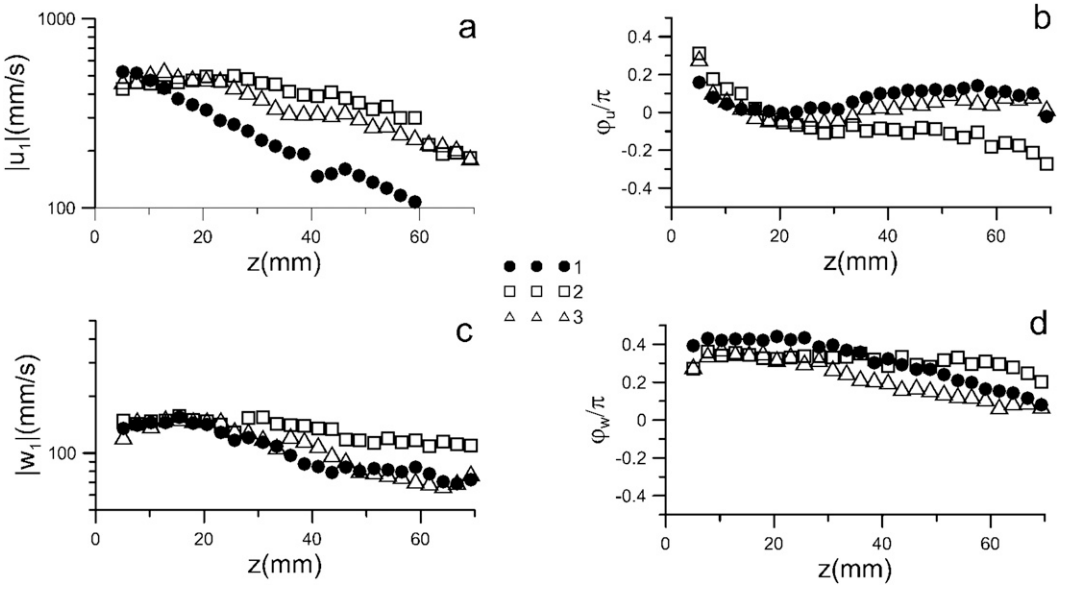

FIG. 21. The profiles of magnitude and phase of the first harmonic of the wave-induced disturbance of the (a),(b) horizontal and (c),(d) vertical velocity component for experiments 1 ($ka = 0.16$), 2 ($ka = 0.3$), and 3 ($ka = 0.25$).

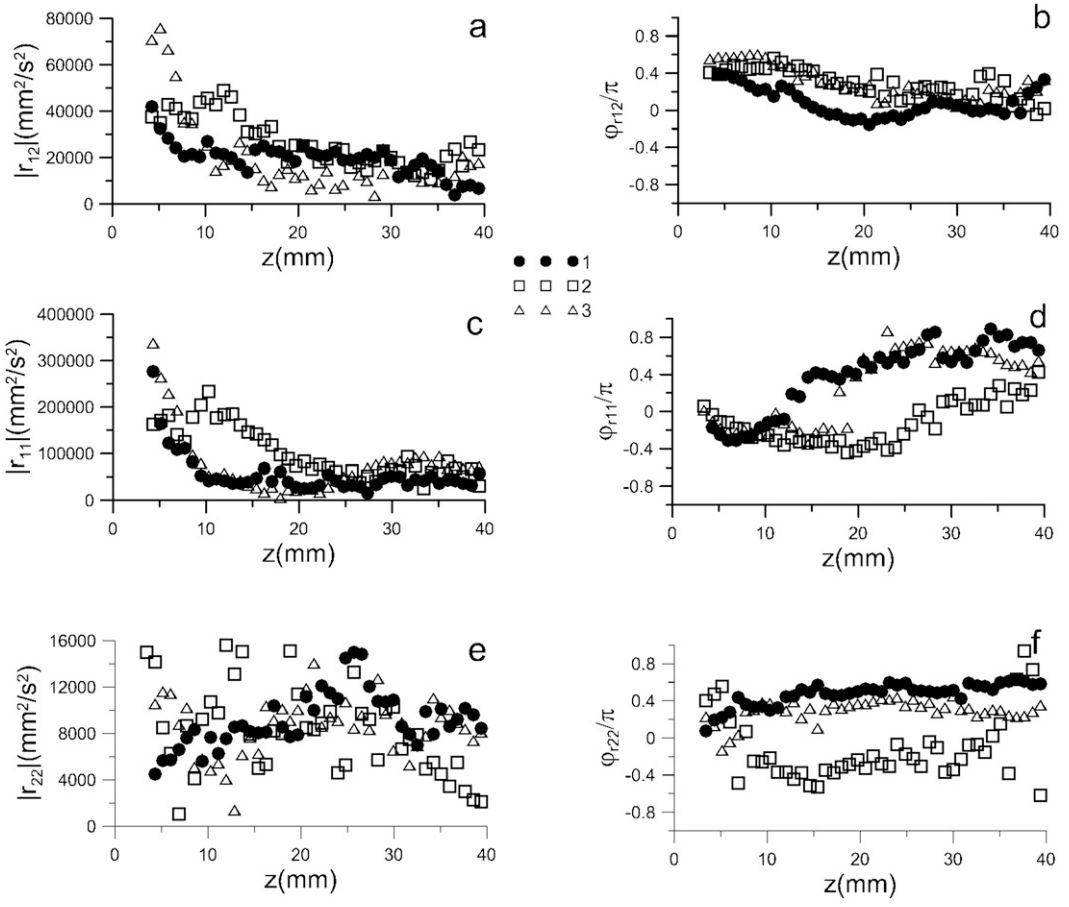

FIG. 22. The profiles of (a),(c),(e) magnitude and (b),(d),(f) phase of the first harmonic of the wave-induced disturbance of the turbulent stresses for experiments 1, 2, and 3.

where $E = \rho_w \omega^2 a^2/(2k)$. Allowance for the kinematic boundary conditions,

$$v|_{y*=0} = \frac{\partial \eta}{\partial x*}(-c), \tag{5.10}$$

and the no-slipping conditions at the water surface,

$$u|_{y*=0} = ck\eta, \tag{5.11}$$

yields

$$\frac{1}{2}\frac{da^2}{dt} = \frac{kc}{\omega^2}\frac{\rho_a}{\rho_w}\left\langle (P-\sigma_{11})\frac{\partial \eta}{\partial x} - c\eta\sigma_{12}\right\rangle\Big|_{y*=0}. \tag{5.12}$$

The estimations show that usually the dominant term in the right-hand side of Eq. (5.12) is the pressure in the phase with a water slope. It can be explained by the expressions for P and σ_{ij} at the water surface. For estimations we can employ the expressions obtained by Benjamin (1959) for the case of laminar airflow over waves, because close to the water surface the turbulent fluctuations vanish. Then, the pressure component in phase with the water slope is

$$P' = \frac{\nu}{ik}\frac{d\chi_1}{d\eta}, \tag{5.13}$$

where χ_1 is the wave disturbance of vorticity. In a laminar flow, σ_{11} and σ_{12} are the viscous stresses and at the water surface the tangential viscous stress dominates,

$$\sigma_{12} = \nu\chi_1. \tag{5.14}$$

Comparing Eqs. (5.13) and (5.14) yields $\sigma_{12}/|P| \sim k\delta$, where δ is a typical vertical scale of wave disturbances, or the scale of the wave turbulent boundary layer. Taking into account the estimation of the eddy viscosity coefficient on the scale δ, $\nu_v = \kappa u_* \delta$, gives $\delta \propto \sqrt{\nu_v/(\kappa c)} \propto (\kappa u_*)/(ck)$ and then $|\sigma_{12}|/|P| \propto [(\kappa u_*)/c]\mathbf{u}$. In this experiment, $(\kappa u_*)/c \propto 1$ (see values of wave celerity c and wind friction velocity u_* in Tables 1, 2), and then the terms containing σ_{12} and σ_{12} can be omitted and the simplified expression for the wave energy flux is valid,

$$\Pi = \rho_a c \langle \mathrm{P}_a \eta_x \rangle \tag{5.15}$$

Then the wave growth rate is

$$\mathrm{Im}\omega = \frac{\omega}{c^2}\frac{\rho_a}{\rho_w}\frac{\langle \mathrm{P}_a \eta_x \rangle}{(ka)^2}. \tag{5.16}$$

Introducing a wind–wave interaction parameter β similar to (Belcher et al. 1994) gives

$$\mathrm{Im}\omega = \frac{1}{2}\frac{u_*^2}{c^2}\beta\frac{\rho_a}{\rho_w}, \tag{5.17}$$

where

$$\beta = \frac{2}{u_*^2}\frac{\langle \mathrm{P}_a \eta_x \rangle}{(ka)^2}.$$

It is related to Plant's (1982) definition of the wind–wave interaction parameter as $\beta_{\mathrm{Plant}} = (\rho_a/\rho_w)\beta$. For Plant's (1982) data, $\beta_{\mathrm{Plant}} = 0.04 \pm 0.02$, $(\rho_a/\rho_w) = 1.25 \times 10^{-3}$, and $\beta = 32 \pm 16$.

Direct contact method of measuring pressure distribution over waves employs the Elliott disk (Elliott 1972; Donelan et al. 1999). Alternatively, pressure distribution can be retrieved from the measurements of the wave-induced velocity components and turbulent stresses using the governing equations for the turbulent flow averaged over the turbulent fluctuations in Eqs. (3.9) and (3.10).

c. *Retrieving the wave-induced pressure field from the velocity measurements*

The method of retrieving the wave-induced disturbances of the mean pressure via velocity field was proposed by Benjamin (1959) for the case of a laminar flow. It can be easily adapted to the case of a turbulent flow. Similarly to Benjamin (1959), integrating Eq. (3.10) for the y momentum component with respect to y^* and taking into account the continuity Eq. (3.11) gives

$$\frac{1}{\rho_a}(\langle p \rangle - \sigma_{22})\Big|_{y*}^{H} = -\int_{y*}^{H}\left[\frac{\partial\langle v\rangle}{\partial t^*} + \frac{\partial}{\partial x^*}(\langle u\rangle\langle v\rangle - \sigma_{12})\right]dy' - \left[\langle v\rangle\left(\langle v\rangle - \langle u\rangle\frac{\partial\eta}{\partial x^*} - \frac{\partial\eta}{\partial t^*}\right) - \sigma_{12}\frac{\partial\eta}{\partial x^*}\right]\Bigg|_{y*}^{H}. \tag{5.18}$$

Alternatively to the original expressions by Benjamin (1959), we integrated a nonlinearized equation for the y momentum component and used a finite upper limit of the integral in Eq. (5.18), because the velocity field in this experiment was measured in a limited area.

According to Eq. (5.8), the energy momentum flux to a harmonic wave is determined by the amplitude and phase of the first harmonic of the wave-induced pressure field. In turn, it follows from Eq. (5.18) that this value is determined by the first harmonic of the right-hand side expression, including the first harmonics of turbulent stress σ_{12} and the momentum flux tensor component $\langle u\rangle\langle v\rangle$ in the integrand and high harmonics of the quantities in the second nonlinear term $-\sigma_{12}(\partial\eta/\partial x^*)$ in the right-hand side of Eq. (5.18). The first nonlinear term $\langle v\rangle[\langle v\rangle - \langle u\rangle(\partial\eta/\partial x^*) - (\partial\eta/\partial t^*)]$ vanishes at the water surface because of the boundary condition in Eq. (3.12).

We compared in Fig. 23 the measured component of the momentum flux tensor $\langle u\rangle\langle v\rangle$ with the linear approximation of this quantity $U\langle v\rangle$. It is seen in the figure that for all experiments, including the cases of steep and breaking waves, the linear approximation is very close to the actual values of the momentum flux at any level from the wavy water surface. However, the measurements presented in section 5a(3) show that the wave-induced disturbances of the tangential stress are substantially nonlinear. Hence, it may be expected that high harmonics of σ_{12} should be taken into account when retrieving the pressure field from measurements of the velocity field. However, the estimates presented below (see Fig. 27) show that the contribution of the turbulent stresses to the wave-induced pressure field is small in comparison with the contribution of the mean flow. This permits using the linearized Eq. (5.18) for calculating the field of normal stresses.

If we represent the first harmonic of the wave-induced disturbances of an air-dynamic quantity $q(x^*, y^*, t^*)$ as $q_{\sim}(x^*, y^*, t^*) = \hat{q}(y^*)e^{-i(\omega t^* - kx^*)}$, then the linearized equation [Eq. (5.18)] yields

$$\hat{p} - \hat{\sigma}_{22}\big|_{y*}^{H} = ik\int_{y*}^{H}[\hat{\sigma}_{12} - (U - c)\hat{v}]\,dy' + [\Sigma_{12}(y^*) - \Sigma_{12}(H)]ik\hat{\eta}. \tag{5.19}$$

The value of $\hat{p}$ at the upper limit $y^* = H$ can be taken from the equation for the x momentum component in Eq. (3.9). Besides, as wave disturbances decrease with the distance from the water surface, the linearized equation

$$ik(U - c)\left(\hat{u} - \hat{\eta}\frac{dU}{dy^*}\right) + \hat{v}\frac{dU}{dy^*} + ik\hat{p} - \frac{\partial\Sigma_{22}}{\partial y^*}ik\hat{\eta} = ik\hat{\sigma}_{11} + \frac{\partial}{\partial y^*}\hat{\sigma}_{12} - \frac{\partial\Sigma_{11}}{\partial y^*}ik\hat{\eta} \tag{5.20}$$

may be applied; then Eq. (5.19) gives

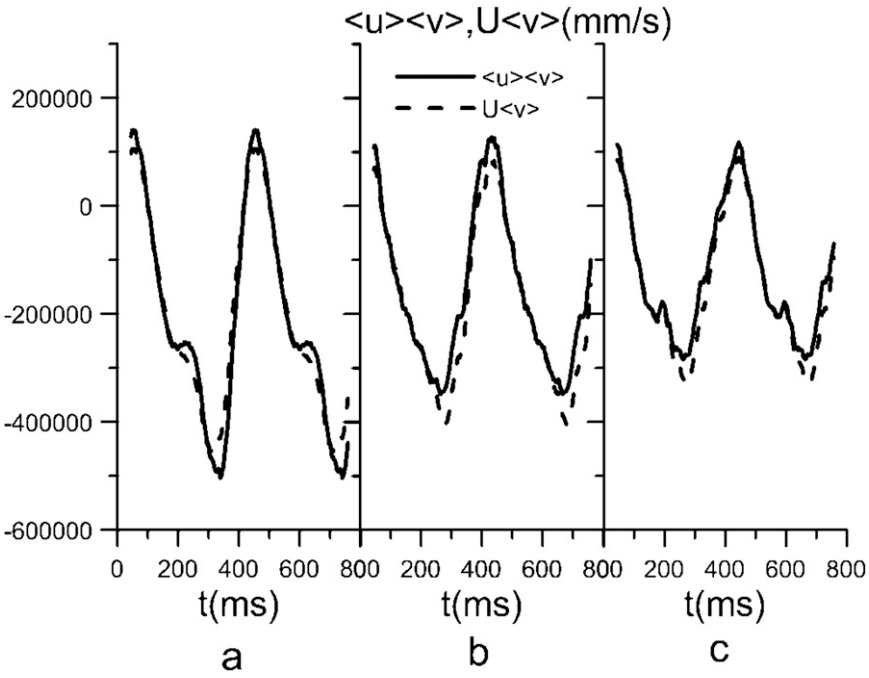

FIG. 23. Component of the momentum flux tensor $\langle u\rangle\langle v\rangle$ and the linear approximation of this value $U\langle v\rangle$ for experiments (a) 1 ($ka = 0.16$), (b) 2 ($ka = 0.3$), and (c) 3 ($ka = 0.25$).

$$\hat{p}(y^*) - \hat{\sigma}_{22}(y^*) = ik\int_{y^*}^{H}[(U-c)\hat{v} - \hat{\sigma}_{12}]\,dy' + [U(H)-c]\left(\hat{\eta}\frac{dU}{dy^*} - \hat{u}\right)\Big|_{y^*=H} - \frac{1}{ik}\hat{v}(H)\frac{dU}{dy^*}\Big|_{y^*=H} + [\Sigma_{12}(H) - \Sigma_{12}(y^*)]ik\hat{\eta} + \hat{\sigma}_{11}(H) + \frac{1}{ik}\frac{d}{dy^*}\hat{\sigma}_{12}(H) + \frac{d(\Sigma_{22}-\Sigma_{11})}{dy^*}\hat{\eta}. \quad (5.21)$$

Here, the upper layer of integration $H = 70$ mm, which is, on one hand, close enough to the water surface to be within the logarithmic part of the turbulent boundary layer and, on the other hand, sufficiently far from the water surface for decreasing wave disturbances, so that $kH > 1$.

Generally, the value of normal stress at $y_* = 0$ required for estimation of the energy flux from and to waves can be expressed by the velocity field in two ways, either by the integral in Eq. (5.21) or by the algebraic expression in Eq. (5.20). The advantage of a more complicated integral form as compared to the algebraic expression was discussed by Benjamin (1959), who emphasized that the integral expression assumes that the ''pressure at the boundary is generated by cumulative action of the disturbance over the whole flow field and is not particularly sensitive to the state of affairs near S (surface). This is a familiar idea in boundary layer theory'' (Benjamin 1959).

The contribution of the viscous boundary layer close to the air–water interface to the integral in Eq. (5.21) at $y^* = 0$ is relatively small. It allows avoiding substantial errors arising when using the algebraic expression in Eq. (5.20), where the major contribution to the normal stress near the water surface is determined by the derivative $\partial\hat{\sigma}_{12}/\partial y$, which cannot be retrieved from the experimental data without substantial errors.

The values of $(\hat{p} - \hat{\sigma}_{22})(0)$ and $\varphi = \arg[(\hat{p} - \hat{\sigma}_{22})(0)]$ can be calculated from the measurements of the wave-induced velocity components and turbulent stresses by the integral expression in Eq. (5.21). Then the wind–wave interaction parameter will be

$$\beta = \frac{|(\hat{p} - \hat{\sigma}_{22})(0)|\sin\varphi}{(ka)u_*^2}. \quad (5.22)$$

It should be mentioned that the dominant term in the right-hand side of Eq. (5.21) is

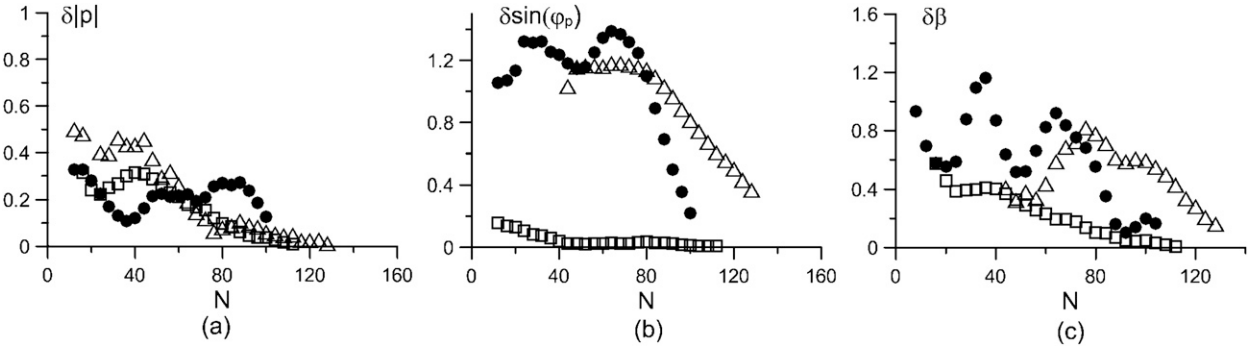

FIG. 24. (a) Convergence of the normalized ensemble-averaged magnitude of wave-induced pressure disturbance, (b) phase shift of wave-induced pressure disturbance, and (c) the corresponding wind–wave interaction parameter for experiments 1 ($ka = 0.16$), 2 ($ka = 0.3$), and 3 ($ka = 0.25$).

$$[U(H) - c]\left(\hat{\eta}\frac{dU}{dy^*} - \hat{u}\right)\Big|_{y^*=H}.$$

For $U(H) > c$, the phase shift of

$$[U(H) - c]\left(\hat{\eta}\frac{dU}{dy^*} - \hat{u}\right)\Big|_{y^*=H}$$

[then $(\hat{p} - \hat{\sigma}_{22})(0)$] is close to 180° and the value of β that is proportional to $\sin\varphi$ is sensitive to the errors in the phase shift and therefore is the major source of errors in β. However, because this term decreases with distance from the surface, the error can be reduced by increasing the range of measurements.

Convergence tests of the measured magnitude $|p|$ and phase shift φ of the first harmonic of wave-induced pressure disturbances and parameter of the air–sea interaction β were conducted for data acquired in all experiments similar to Melville et al. (2002). A total sample of 100–120 repeats was used for these tests. The normalized errors in the statistical estimates p_N, φ_N, and β_N in the Nth series, $\delta\beta N$, are defined as follows:

$$\delta p_N = \frac{\big||p|_N - |p|\big|}{|p|},$$

$$\delta \sin\varphi_N = \frac{|\sin\varphi_N - \sin\varphi|}{|\sin\varphi|}, \quad \text{and}$$

$$\delta\beta_N = \frac{|\beta_N - \beta|}{|\beta|}.$$

Figure 24 shows that for 100 series the normalized error in the mean pressure disturbance magnitude (Fig. 24a) is approximately 10% in all experiments. The error in $\sin\varphi$ (Fig. 24b) is about 10% in experiment 2 ($ka = 0.3$) for 100 series; 20% in experiment 1 ($ka = 0.16$) for 100 series; and about 25% in experiment 3 ($ka = 0.25$) for 120 series, when referred to an ensemble of 136 repeats. Increasing of the normalized error in sine of phase shift in experiments 1 and 3 is related to φ_N tending to π and then $\sin\varphi$ tending to 0 (Fig. 24b). Increasing of normalized error in $\sin\varphi$ gives rise to increased (about 25%) errors in β for experiments 1 and 3 (Fig. 24c), and the error in β in the second experiment is less than 10%.

The vertical profiles of magnitude and phase of $(\hat{p} - \hat{\sigma}_{22})(y^*)$ are presented in Figs. 25a,b. Figure 25c shows the dependence of the normalized imaginary part of $(\hat{p} - \hat{\sigma}_{22})(y^*)$ along the vertical coordinate. It is clear that the scale of function $(\hat{p} - \hat{\sigma}_{22})(y^*)$ is on the order of $1/k$; that is, it substantially exceeds the scale of the wave boundary layer, so $p(0)$, which determines β according to Eq. (5.22) can be easily estimated by the linear extrapolation to $y^* = 0$.

The curve for β as a function of the wave slope ka is plotted in Fig. 26a. With the estimated errors of the experimental measurements, the statistical estimates of β are within the interval of Plant's (1982) approximation. At the same time, the experimental errors do not permit retrieving the statistically significant dependence of β on ka, but a slight decrease of β with an increase in the wave slope can be noticed.

The phase shift between the normal stress and surface elevation is plotted in Fig. 26b. It is clear that $\varphi < \pi$ and the difference between π and φ grows with increasing slope of the wave.

The integral expression in Eq. (5.21) suggests the physical interpretation of the components contribution in the pressure at the air–water interface proposed by Benjamin (1959). The term

$$P_1(y^*) = ik\int_{y^*}^{H}[(U - c)\hat{v}]\,dy' + [U(H) - c] \times \left(\hat{\eta}\frac{dU}{dy^*} - \hat{u}\right)\Big|_{y^*=H} - \frac{1}{ik}\hat{v}(H)\frac{dU}{dy^*}\Big|_{y^*=H} \tag{5.23}$$

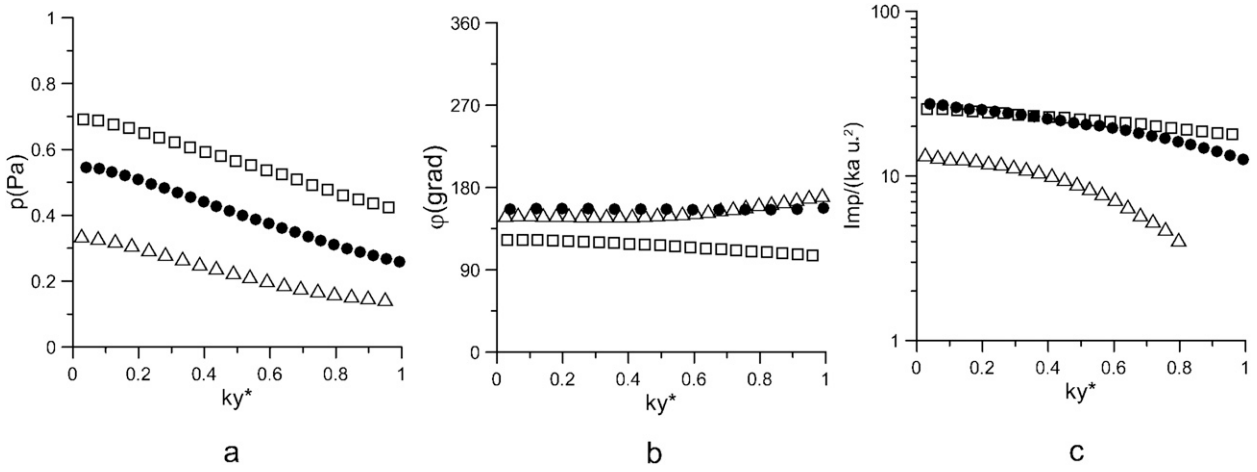

FIG. 25. Vertical profiles of (a) magnitude and (b) phase of $(\hat{p} - \hat{\sigma}_{22})(y^*)$. (c) The dependence of the normalized imaginary part of $(\hat{p} - \hat{\sigma}_{22})(y^*)$ on the vertical coordinate.

represents the contribution of the wave flow disturbances averaged over turbulent fluctuations to the surface pressure. The term

$$P_2(y^*) = ik\int_{y^*}^{H}(-\hat{\sigma}_{12})\,dy' + [\Sigma_{12}(H) - \Sigma_{12}(y^*)]ik\hat{\eta} + \hat{\sigma}_{11}(H) + \frac{1}{ik}\frac{d}{dy^*}\hat{\sigma}_{12}(H) + \frac{d(\Sigma_{22} - \Sigma_{11})}{dy^*}\hat{\eta} \tag{5.24}$$

describes the contribution of the cumulative effect of the tangential turbulent stress.

The contributions of P_1 and P_2 to parameter β are plotted in Fig. 27. The experimental errors are substantial, so we can estimate only the order of magnitude of the term P_2. Comparison of P_1 and P_2 (Fig. 27) shows that the cumulative effect of wave disturbances averaged over turbulence dominates over the contribution of turbulent stresses substantially, so that the latter is negligible within the experimental errors. We suppose that this could be a possible explanation for a rather weak sensitivity of parameter β to the model used for its calculation, so even the quasi-laminar model proposed by Miles (1957, 1959) is in a reasonable agreement with numerous experimental data (see Janssen 1991, and references therein). In section 6, we use for the theoretical analysis of the obtained data a relatively simple model of the wave turbulent boundary layer, based on the Reynolds equations closed within the first-order hypothesis.

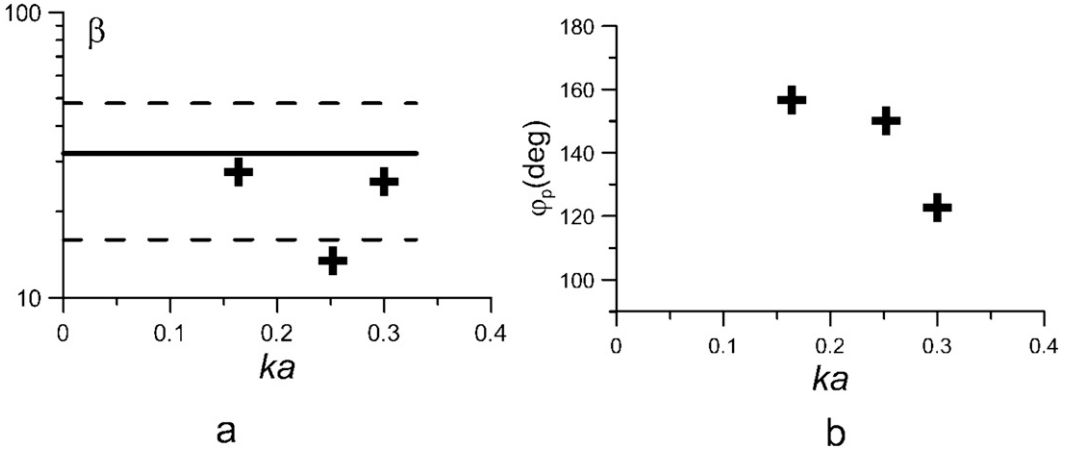

FIG. 26. Dependence of (a) β and (b) the phase shift of the main harmonic of the wave-induced normal stress on the wave steepness.

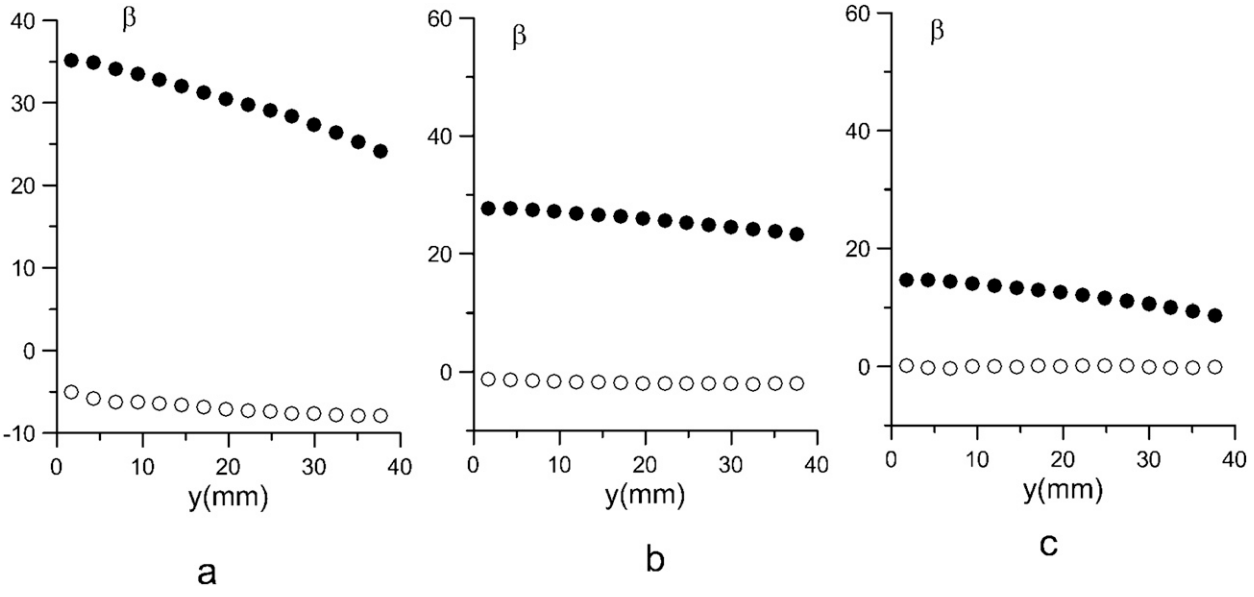

FIG. 27. Contribution of the cumulative effect of the averaged velocity disturbances (closed symbols) and tangential turbulent stress (open symbols) in parameter β for experiments (a) 1 ($ka = 0.16$), (b) 2 ($ka = 0.3$), and (c) 3 ($ka = 0.25$).

6. The quasi-linear model of turbulent wind over the wavy water surface

We compared the experimental data with the predictions of the quasi-linear model for a turbulent boundary layer over the wavy water surface developed by Reutov and Troitskaya (1995). The model is similar to the earlier models proposed by Gent and Taylor (1976), Al-Zanaidi and Hui (1984), Jenkins (1992), and van Duin and Janssen (1992). These models are quasi stationary; they assume conservation of the momentum in the boundary layer above the water surface,

$$\tau_{\text{turb}}(z) + \tau_{\text{wave}}(z) = u_*^2, \tag{6.1}$$

where $\tau_{\text{wave}}(z)$ is the wave momentum flux and $\tau_{\text{turb}}(z)$ is the turbulent momentum flux in the turbulent boundary layer.

Within the quasi-linear model applied here, the wind is regarded to be a turbulent boundary layer over the wavy water surface described within the first-order semiempirical model of turbulence based on the set of the Reynolds equations,

$$\frac{\partial\langle u_i\rangle}{\partial t} + \langle u_j\rangle\frac{\partial\langle u_i\rangle}{\partial x_j} + \frac{1}{\rho_a}\frac{\partial\langle p\rangle}{\partial x_i} = \frac{\partial\sigma_{ij}}{\partial x_j}, \tag{6.2}$$

and the following expressions for the tensor of turbulence stresses:

$$\sigma_{ij} = \langle u_i' u_j'\rangle = \nu\left(\frac{\partial\langle u_i\rangle}{\partial x_j} + \frac{\partial\langle u_j\rangle}{\partial x_i}\right). \tag{6.3}$$

Here, $\langle\ \rangle$ denotes the quantities averaged over turbulent fluctuations and ν is the turbulent viscosity coefficient that is a given function of z. We use a self-similar expression for the eddy viscosity coefficient in the turbulent boundary layer,

$$\nu = \nu_a f\left(\frac{\eta\sqrt{\tau_{\text{turb}}}}{u_*^2}\right), \tag{6.4}$$

where ν_a is the air molecular viscosity.

We used the approximation for f obtained by Smolyakov (1973) on the basis of the laboratory experiments on a turbulent boundary layer. Finally, the expression for $\nu(z)$ takes the form

$$\nu = \nu_a\left\{1 + \kappa\frac{u_*\eta\sqrt{1 - \tau_{\text{wave}}/u_*^2}}{\nu_a} \times\left[1 - e^{-1/L(u_*\eta/\nu_a)^2(1-(\tau_{\text{wave}}/u_*^2))}\right]\right\}. \tag{6.5}$$

In this expression, L is a number that determines the scale of the viscous sublayer of a turbulent boundary layer; it depends on the regime of the flow over the surface. Comparison with the parameters of the velocity profile in the turbulent boundary layer from Miles (1959) gives $L = 22.4$ for a hydrodynamically smooth surface, $L = 13.3$ for the transition regime of a flow over the surface, and $L = 1.15$ for a rough surface.

The boundary conditions at the air–sea interface $z = \xi(x, y, t)$ are

$$\frac{\partial \xi}{\partial t} + \langle u \rangle \frac{\partial \xi}{\partial x} + \langle v \rangle \frac{\partial \xi}{\partial y}\bigg|_{z=\xi(x,y,t)} = \langle w \rangle|_{z=\xi(x,y,t)} \quad \text{and} \tag{6.6}$$

$$\langle \mathbf{u}_\tau^w \rangle|_{z=\xi(x,y,t)} = \langle \mathbf{u}_\tau^a \rangle|_{z=\xi(x,y,t)}, \tag{6.7}$$

where $\langle u \rangle$ and $\langle v \rangle$ are the x and y components of the velocity field in the air, averaged over turbulent fluctuations, and $\langle \mathbf{u}_\tau^w \rangle|_{z=\xi(x,y,t)}$ and $\langle \mathbf{u}_\tau^a \rangle|_{z=\xi(x,y,t)}$ are the tangential velocity components in water and in air.

To avoid strong geometric nonlinearity, the transformation to the wave-following orthogonal curvilinear coordinates is performed,

$$x = \xi - ae^{-k\eta} \sin k\xi \quad \text{and} \tag{6.8}$$

$$z = \eta + ae^{-k\eta} \cos k\xi. \tag{6.9}$$

For the case of one harmonic at the water surface, the mean flow disturbances are 2D, so the streamfunction Φ can be introduced,

$$u = \frac{\partial \Phi}{\partial z}, \quad w = -\frac{\partial \Phi}{\partial x}, \tag{6.10}$$

and the Reynolds equations can be formulated in terms of streamfunction Φ and vorticity χ (see Reutov and Troitskaya 1995),

$$\frac{\partial \chi}{\partial t} + \frac{1}{I}\frac{\partial \chi}{\partial \xi}\left(\frac{\partial \Phi}{\partial \eta}\right) - \frac{1}{I}\frac{\partial \chi}{\partial \eta}\left(\frac{\partial \Phi}{\partial \xi}\right) = \Delta(\nu\chi) - \frac{2}{I^2}\nu_{\eta\eta}\frac{\partial^2 \Phi}{\partial \xi^2} - \frac{I_\eta}{I^3}[(\Phi_\eta \nu_\eta)_\eta - \nu_\eta \Phi_{\xi\xi}] - \frac{I_\xi}{I^3}(2\nu_\eta \Phi_{\xi\eta} - \Phi_\xi \nu_{\eta\eta}) + \Phi_\eta \nu_\eta \frac{I_\xi^2 + I_{\eta\xi}^2}{I^4} \quad \text{and} \tag{6.11}$$

$$\chi = \Delta\Phi. \tag{6.12}$$

The wind–wave interaction is considered here in the quasi-linear approximation similar to the approach developed by Jenkins (1992) and Janssen (1991), where disturbances induced in the airflow by the waves at the water surface were described in the linear approximation. No strong nonlinear effects (e.g., flow separation) are taken into account for the disturbances averaged over turbulent fluctuations. The applicability of this approach to the conditions of our experiments can be justified by the observed smoothness of the averaged velocity fields in the airflow over waves even for steep and breaking waves.

We now seek a solution to the system as a superposition of the mean field and harmonic wave disturbance,

$$\Phi = \Phi_0(\eta) + \Phi_1(\eta)e^{ik\xi} \quad \text{and} \tag{6.13}$$

$$\chi = X_0(\eta) + X_1(\eta)e^{ik\xi}. \tag{6.14}$$

Equations for the complex amplitudes $\Phi_1(\eta)$ and $\chi_1(\eta)$ are obtained by linearizing the system in Eqs. (6.11) and (6.12),

$$(\Phi_{0\eta}X_1 - \Phi_1\chi_{0\eta})ik - \left(\frac{d^2}{d\eta^2} - k^2\right)(X_1\nu) = -2\nu_\eta \Phi_1 k^2 - 2kae^{-k\eta}(\Phi_{0\eta}\nu_\eta)_\eta \quad \text{and} \tag{6.15}$$

$$\frac{d^2\Phi_1}{d\eta^2} - k^2\Phi_1 = X_1 - 2kae^{-k\eta}X_0, \tag{6.16}$$

where $\Phi_{0\eta} = d\Phi_0/d\eta$.

We consider solutions to the system in Eqs. (6.15) and (6.16) to be decreasing at large distances from the surface. The boundary conditions at the water surface for the system in Eqs. (6.15) and (6.16) follow from Eqs. (6.6) and (6.7) expressed in the curvilinear coordinates (for details, see Reutov and Troitskaya 1995),

$$\Phi_1|_{\eta=0} = 0 \quad \text{and} \tag{6.17}$$

$$\Phi_{1\eta}|_{\eta=0} = 2cka. \tag{6.18}$$

The solution to the system in Eqs. (6.15) and (6.16) allows calculating the wind growth rate of the surface wave, which is proportional to the vertical energy flux in the wave disturbance at the water surface,

$$\mathrm{Im}\omega = \frac{k}{2}\frac{\rho_a}{\rho_w}\frac{\overline{(p - \sigma_{11})w - u\sigma_{12}}^T}{(kac)^2}, \tag{6.19}$$

where p is the wave disturbance of the pressure in the air at the water surface, σ_{ij} are the wave disturbances of turbulent stresses, and the symbol $\overline{\ \ \ }^T$ denotes averaging over a wave period. Using the expressions for the complex amplitudes of pressure and turbulent stresses via vorticity gives the expression for the wind–wave growth rate,

$$\mathrm{Im}\omega = -\frac{1}{2}\frac{\rho_a}{\rho_w}\nu \mathrm{Re}\left(\frac{X_{1\eta} - kX_1}{kac}\right)\bigg|_{\eta=0} = \frac{1}{2}\left(\frac{u_*}{c}\right)^2 \beta\omega; \tag{6.20}$$

β was defined above as the wind–wave interaction parameter.

The only nonlinear effect taken into account in the quasi-linear approximation is the wave momentum flux arising from demodulation of the wave disturbances induced in the airflow by waves at the water surface,

$$\frac{d^2}{d\eta^2}(\nu\chi_0) = k\frac{d}{d\eta}kae^{-k\eta}\nu_\eta \mathrm{Re}(\psi_{1\eta} - k\psi_1) - 2(ka)^2e^{-2k\eta}\nu_\eta\Phi_{0\eta} + \frac{1}{2}k\frac{d}{d\eta}\mathrm{Im}(\psi_1^*\chi_1) \equiv -\frac{d^2\tau_{\mathrm{wave}}}{d\eta^2} \quad \text{and} \tag{6.21}$$

$$\frac{d\Phi_{0\eta}}{d\eta} = \chi_0[1 + (ka)^2e^{-2k\eta}] - kae^{-k\eta}\mathrm{Re}\chi_1, \tag{6.22}$$

with the boundary conditions

$$\nu\chi|_{\eta\to\infty} = u_*^2 \quad \text{and} \quad \Phi_{0\eta}|_{\eta=0} = -c. \tag{6.23}$$

Equations (6.21) and (6.22) express the momentum balance condition in the air turbulent boundary layer in terms of the wave fields induced in the airflow. The momentum balance equation similar to Eq. (6.1) easily follows from Eq. (6.21) by double integration with respect to η,

$$\nu\chi_0(\eta) + \tau_{\mathrm{wave}}(\eta) = u_*^2,$$

where

$$\tau_{\mathrm{wave}}(\eta) = k\int_\infty^\eta \left[\nu_\eta \mathrm{Re}(\psi_{1\eta} - k\psi_1)kae^{-k\eta} + 2(ka)^2e^{-2k\eta}\nu_\eta\Phi_{0\eta} - \frac{1}{2}\mathrm{Im}(\psi_1^*\chi_1)\right]d\eta \tag{6.24}$$

is the wave momentum flux. This term contributes to the mean wind velocity giving rise to dynamical roughness determined by the wave–airflow interaction.

7. Comparison between theory and experiment for the wind and wave parameters retrieved from the experimental data

The main purpose of comparing the theoretical predictions and experimental data is to verify two main physical assumptions underlying this model, (i) applicability of the model [Eq. (6.5)] for the eddy viscosity in the smooth flow over the water surface and (ii) quasi-linear approximation for the wind–wave interaction. The wind and wave parameters retrieved from the experimental data were employed as an input in calculations within the model.

The theoretical model is formulated in coordinates (ξ, η) [Eqs. (6.8) and (6.9)], whereas the experimental data are presented in coordinates (x^*, y^*) [Eq. (3.8)]. To enable comparison between the theoretical calculations and the experimental data, they should be expressed in equal coordinates. For this purpose, we perform transformation from coordinates (ξ, η) [(Eqs. (6.8) and (6.9)] to coordinates (x^*, y^*) [Eq. (3.8)]. In the curvilinear coordinates [Eqs. (6.8) and (6.9)], the water surface curved by the wave $\eta = 0$ can be expressed in coordinates (x, y) as the following parametric function:

$$x = \xi - a\sin k\xi \quad \text{and} \tag{7.1}$$

$$z = a\cos k\xi. \tag{7.2}$$

In turn, coordinates (x, y^*) are expressed by (ξ, η) as follows:

$$x = \xi - ae^{-k\eta}\sin k\xi, \tag{7.3}$$

$$x = \xi_1 - a\sin k\xi_1, \quad \text{and} \tag{7.4}$$

$$y^* = \eta + a(e^{-k\eta}\cos k\xi - \cos k\xi_1). \tag{7.5}$$

The values measured in the experiment were calculated within the quasi-linear model in coordinates (ξ, η) and then recalculated to the grid (x^*, y^*) based on the parametric expressions in Eqs. (7.3)–(7.5); after that, the theoretical calculations were compared with the experimental data.

The Cartesian components of the velocity vector are expressed via a streamfunction formulated in curvilinear coordinates (ξ, η) as

$$u = \frac{\partial\psi}{\partial y} = \left(\frac{\partial\psi}{\partial\eta}\frac{\partial y}{\partial\eta} + \frac{\partial\psi}{\partial\xi}\frac{\partial y}{\partial\xi}\right)\frac{1}{I} \quad \text{and} \tag{7.6}$$

$$w = -\frac{\partial\psi}{\partial x} = -\left(\frac{\partial\psi}{\partial\eta}\frac{\partial x}{\partial\eta} + \frac{\partial\psi}{\partial\xi}\frac{\partial x}{\partial\xi}\right)\frac{1}{I} \tag{7.7}$$

Expressing coordinates (x^*, y^*) via (ξ, η) by Eqs. (7.3)–(7.5) and averaging over x^* gives the mean velocity profile $U_0(y^*)$ that can be directly compared with the measured data [see Eq. (5.3.)].

To perform comparison with the experiment, we calculated the turbulent tangential stress $\langle u'w'\rangle$, expressed it in the grid (x^*, y^*) within the model, and then averaged it over x^*. The gradient closing hypothesis yields the following expressions for $\langle u'w'\rangle(x^*, y^*)$ via the

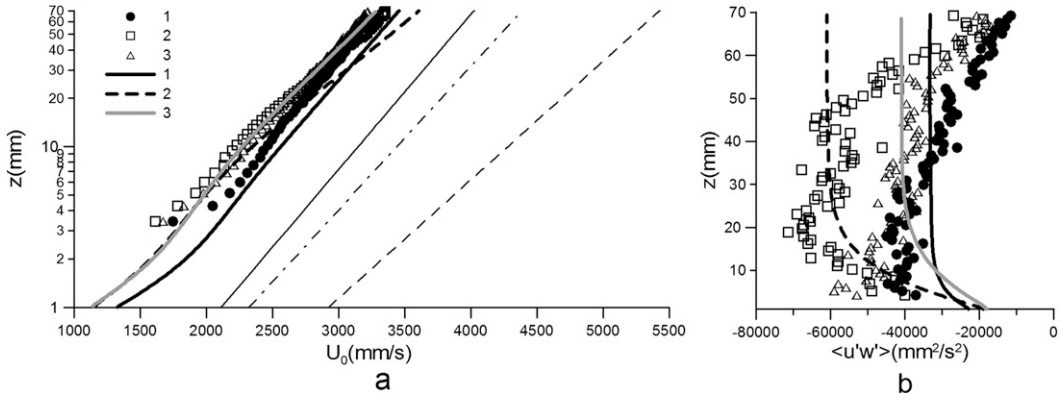

FIG. 28. Comparing theory and experiment: (a) the mean velocity profile and (b) the stress profile. The filled circle, open box, and open triangle symbols correspond to experiments 1, 2, and 3, respectively. The bold curves are $u_* = 180$ mm s^{-1} and $ka = 0.16$ (1); $u_* = 240$ mm s^{-1} and $ka = 0.3$ (2); and $u_* = 200$ mm s^{-1} and $ka = 0.25$ (3).

velocity components $\langle u\rangle$ and $\langle w\rangle$ or streamfunction ψ and vorticity χ,

$$\langle u'w'\rangle = \nu\left(\frac{\partial\langle u\rangle}{\partial z} + \frac{\partial\langle w\rangle}{\partial x}\right) = \nu\left(\frac{\partial^2\psi}{\partial z^2} - \frac{\partial^2\psi}{\partial x^2}\right) = \nu\left(\chi - 2\frac{\partial^2\psi}{\partial x^2}\right). \tag{7.8}$$

In the curvilinear coordinates (ξ, η), we have

$$\frac{\partial^2\psi}{\partial x^2} = \left(\frac{\partial x}{\partial\xi}\right)^2\chi + \frac{\partial^2\psi}{\partial\xi^2}\frac{1}{I}\left[\left(\frac{\partial x}{\partial\xi}\right)^2 - \left(\frac{\partial x}{\partial\eta}\right)^2\right] + 2\frac{\partial^2\psi}{\partial\xi\partial\eta}\frac{\partial x}{\partial\xi}\frac{\partial x}{\partial\eta}\frac{1}{I} + \frac{\partial\psi}{\partial\xi}\left[\frac{2}{I}\frac{\partial I}{\partial\xi} - \frac{1}{I^2}\frac{\partial x}{\partial\xi}\left(\frac{\partial I}{\partial\xi}\frac{\partial x}{\partial\xi} + \frac{\partial I}{\partial\eta}\frac{\partial x}{\partial\eta}\right)\right] + \frac{\partial\psi}{\partial\eta}\left[\frac{2}{I}\frac{\partial I}{\partial\eta} - \frac{1}{I^2}\frac{\partial x}{\partial\eta}\left(\frac{\partial I}{\partial\xi}\frac{\partial x}{\partial\xi} + \frac{\partial I}{\partial\eta}\frac{\partial x}{\partial\eta}\right)\right]. \tag{7.9}$$

Expressing coordinates (x^*, y^*) via (ξ,η) according to the expressions in Eqs. (7.3)–(7.5) and averaging the result over x^* yields the theoretical profile of the mean turbulent stress $\overline{\langle u'w'\rangle(y^*, x^*)}^{x}$.

The profiles of the mean velocity and tangential turbulent stress are plotted in Fig. 28. The symbols represent the experimental data described above; the bold curves are obtained within the quasi-linear model described in section 6, thin curves similarly to Fig. 16a present velocity profiles calculated for the case of smooth plane. It is clear that the model calculations are in reliable agreement with the experimental data. The worst agreement between the theory and the experimental data is observed for the first experiment ($ka = 0.16$, smooth wave): the normalized difference between the experimental and theoretical values of the turbulent stress, $(\langle u'v'\rangle_{\text{exp}} - \langle u'v'\rangle_{\text{theor}})/\langle u'v'\rangle_{\text{theor}} = 0.19$, although, it is close to the normalized error in statistical estimate (see section 5a and Fig. 16e).

Figure 29 shows the profiles of theoretical and experimental magnitudes and phases of the main harmonic of wave-induced disturbances of the velocity components. The best agreement between theory and experiment is achieved for small amplitudes of the water wave (experiment 1), and it is quite reasonable even for steep and breaking waves (experiments 2 and 3) (see Fig. 29). It should be emphasized that, in spite of the unharmonic character of the wave-induced disturbances in the airflow, the first harmonic is in reliable agreement with the quasi-linear theory. In these experiments, $U/c = 5.4$–3.8; that is, it is greater than 1. Then, according to the potential theory that is valid for constant airflow velocity, the horizontal component of the wave-induced velocity should be in phase with the water elevation and the phase shift of the vertical component should be $\pi/2$. The theoretical and experimental results both have phase shifts close to these values (Figs. 29b,d). A deviation from this value is caused either by turbulent stresses or by mean flow velocity shear.

We also compared the theoretical predictions for the wave-induced pressure at the water surface and the related parameters. The experimental and theoretical curves for the wind–wave interaction parameter β versus the slope of a paddle-generated wave, including the cases of smooth, steep, and breaking waves are plotted in Fig. 30a. The theoretical curves were calculated for fixed values of wind friction velocity u_* and wave celerity c as functions of wave steepness. The theoretical dependence obtained within the quasi-linear model is in agreement with the experimental data within the estimated experimental error. Both the theoretical and experimental data lie within the confidence interval of

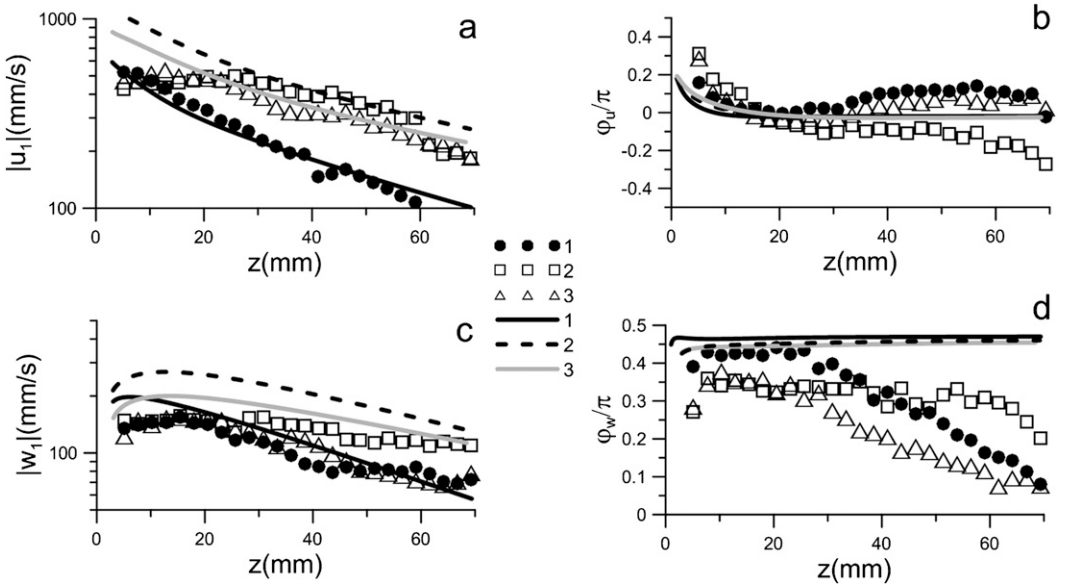

FIG. 29. Profiles of the (a),(c) amplitudes and (b),(d) phases of wave-induced disturbances of the (a),(b) horizontal and (c),(d) vertical velocity components averaged over turbulent fluctuations. The filled circle, open box, and open triangle symbols correspond to experiments 1, 2, and 3, repsectively. The curves are $u_* = 180$ mm s^{-1} and $ka = 0.16$ (1); $u_* = 240$ mm s^{-1} and $ka = 0.3$ (2); and $u_* = 200$ mm s^{-1} and $ka = 0.25$ (3).

Plant's (1982) approximation. The theoretical and experimental parameter β decreases slightly with the wave slope, for both the smooth and steep or breaking wave. The theoretical and experimental curves for the pressure phase shift versus wave slope are plotted in Fig. 30b. The theoretical curve is in a good agreement with the experimental data and yields a monotonously decreasing dependence of the pressure phase shift on wave slope. The plots for the normalized magnitude of the main harmonic of pressure disturbance on the water surface $|p|/(ka)^2$ are presented in Fig. 30c. The sloping-down theoretical curves are in good quantitative agreement with the experimental data.

Because the wave phase velocity is less than the wind speed far from the air–water interface, one can expect existence of a critical level, the height where airflow velocity coincides with wave phase speed. In the neighborhood of the critical level, the pattern of the flow with closed streamlines (the critical layer) occurs in the wave-following reference frame. The scale of the critical layer is determined by wave amplitude and mean flow shear (see Maslowe 1986). In the critical layer, intensive interaction of wave disturbances with mean flow occurs similarly to the interaction of particles and waves in plasma (Fabrikant 1976; Reutov 1980; Janssen 1982). Within the Miles quasi-laminar model, this interaction

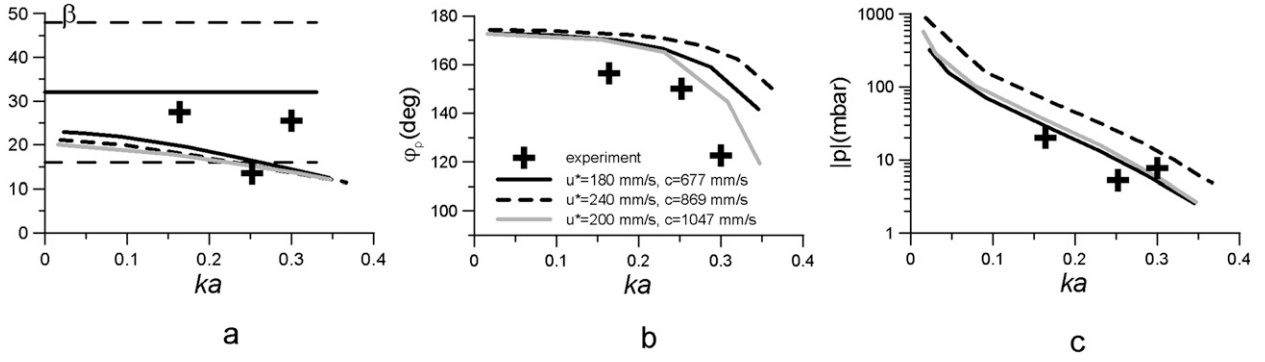

FIG. 30. Comparing theory and experiment: dependence of (a) β, (b) the phase shift, and (c) normalized magnitude of pressure wave disturbance at the water surface on the steepness of the wave.

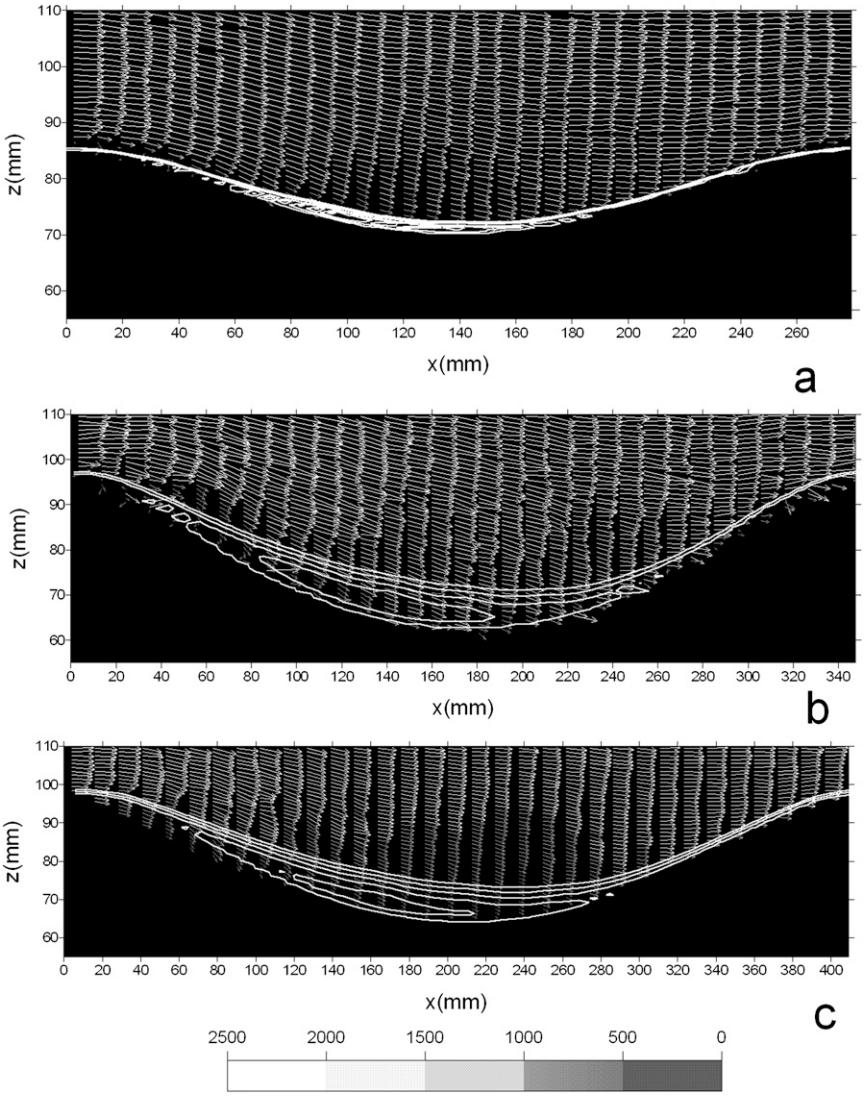

FIG. 31. Theoretically calculated streamlines of the airflow with wave-induced disturbance (curves) and velocity vector field in the wave-following reference frame: (a) $u_* = 180$ mm s^{-1} and $ka = 0.16$; (b) $u_* = 240$ mm s^{-1} and $ka = 0.3$; and (c) $u_* = 200$ mm s^{-1} and $ka = 0.25$.

is the only reason for the wave growth due to the action of wind. In the presence of turbulent stresses, the effects of eddy viscosity contaminate the resonance interaction. Besides, for steep waves the position of the critical level can be effectively below the wave crests, as was the case in our experiments. An example of closed streamlines near the water surface, calculated within the quasi-linear model, is plotted in Fig. 31 along with the vector plot of the airflow velocity presented in the wave-following reference frame. In that experiment, the space resolution was insufficient for detecting details of the structure of the critical layer, which had been predicted to exist at a distance of 1 mm from the water surface. At the same time, we observed an area of reduced airflow velocities close to the water surface that was shifted in phase to the leeward slope of the wave, which coincided with the area of the closed streamlines (Fig. 31).

8. Conclusions

The wind flow over steep and breaking water waves is of considerable interest in terms of modeling and parameterization of momentum, mass, and heat transfer between the atmosphere and the ocean. This problem is very complicated for theoretical and numerical treatment, although the numerical experiments on large eddy simulation of wind turbulence over large-scale waves were recently made by Sullivan et al. (2008). There were

also several laboratory experimental studies of airflow patterns over water waves (e.g., Banner and Melville 1976; Kawai 1981, 1982; Weissmann 1986; Kawamura and Toba 1988; Banner 1990; Reul et al. 1999, 2008; Veron et al. 2007). One of the promising trends in these investigations is application of the techniques based on visualization of the airflow by means of micron-size particles scattering light. Kawai (1981, 1982) used such a technique on the basis of film photography and revealed signatures of airflow separation over the crests of steep water waves in instantaneous images of the flow. Significant progress in such studies has been achieved by Reul et al. (1999, 2008) and Veron et al. (2007) through application of the PIV technique (Adrian 1991). They obtained detailed instant two-dimensional vector velocity fields in the airflow over waves, retrieved the field of the transversal vorticity component and patterns of streamlines projections. Those studies showed that the pattern of an instant airflow over wind wave is characterized by a zone of flow separation near the crest of the wave and reattachment at the windward side of the wave profile.

However, wind over waves is a turbulent stochastic nonstationary flow, and the problems of wind–wave interaction require statistical averaging. The main objective of this paper is the investigation of the statistical properties of airflow over waves, when the effect of flow separation is present in instant flow images. The statistical ensemble for averaging was obtained by means of high-speed video filming at the rate of 1000 frames per second and successive processing by the PIV algorithm. Individual flow patterns manifested typical features of flow separation similar to those obtained by Kawai (1981, 1982), Reul et al. (1999, 2008), and Veron et al. (2007). The average parameters were retrieved by phase averaging of the individual vector fields. The averaged flow patterns were smooth and slightly asymmetrical, with the minimum of the horizontal velocity near the water surface shifted to the leeward of the wave profile.

The results of the measurements were compared with the calculations within the theoretical model of a turbulent boundary layer developed by Reutov and Troitskaya (1995). The model is based on the system of Reynolds equations with the first-order closing hypothesis. The wind–wave interaction is considered within the quasi-linear approximation; that is, wave-induced disturbances in the airflow are considered in the linear approximation, but the resistive effect of the wave momentum flux on the mean flow velocity profile is taken into account. The mean airflow over waves within the model is treated as a nonseparated one: in this case, it is similar to nonseparated wave generation and growth models like, for example, those proposed by Miles (1957, 1962), Valenzuela (1976), van Duin and Janssen (1992), Jenkins (1992), Belcher and Hunt (1993), and Belcher (1999). The wave parameters (wavelength, celerity, and steepness) used in this comparison of theory with experiment were retrieved from the same video films as the ones used for the airflow velocity calculations. The model calculations were in a good agreement with the experimentally measured and conditionally averaged mean wind velocity, turbulent stress, and also amplitude and phase of the main harmonics of the wave-induced velocity components.

Using the obtained statistical ensemble of wind flow velocities, we retrieved the main harmonic of the wave-induced pressure disturbances in the airflow, which determines the energy flux to the water waves. The method of data processing is based on integral expressions similar to those suggested by Benjamin (1959) for the case of a laminar flow, which define the cumulative action of disturbances over the whole flow field and are insensitive to the fine structure of the flow very close to the water surface (e.g., in the viscous sublayer). The retrieved pressure disturbances permitted estimating the energy flux from wind to waves and the wind–wave interaction parameter β. The estimated values of β were found within the interval of Plant's (1982) approximation and slightly decreased with increasing steepness of the wave, in agreement with the theoretical calculations.

Applicability of the nonseparating quasi-linear theory for description of average fields in the airflow over steep and even breaking waves, when the effect of separation is manifested in the instantaneous flow images, can possibly be explained qualitatively by the strongly nonstationary character of the separation process with the typical time being much less than the wave period and by the small scale of flow heterogeneity in the area of separation. In such a situation, small-scale vortices produced within the separation bubble affect the mean flow and wind-induced disturbances as eddy viscosity. Then, the flow turbulence affects the averaged fields as a very viscous fluid. The estimates (see section 3b) show that the effective Reynolds number for the average fields determined by the eddy viscosity has the value $\sim ka < 1$ even for steep waves. It follows from this assumption that strongly nonlinear effects such as flow separations should not be expected in the flow averaged over turbulent fluctuations, and the main harmonics of the wave-induced disturbances of the averaged flow, which determine the energy flux to surface waves, can be described in the weakly nonlinear approximation.

Acknowledgments. We are grateful to Prof. G. Golitsyn, Dr. P. Janssen, Prof. M. Donelan, Dr. A. Babanin, Dr. V. Polnikov, Prof. A. V. Gaponov-Grekhov, and Dr. S. Ermakov for helpful discussions, and to the anonymous

referee whose constructive comments help us to significantly improve the paper. We are also grateful to the master students A. Kandaurov and G. Baidakov for valuable assistance in data processing. This work was supported by grants from RFBR (Projects 09-05-00779a, 07-05-00565a, 07-05-12011, 08-05-97011, 08-05-97013, 06-05-64473, and 10-05-00339-a).

REFERENCES

Adrian, R. J., 1991: Particle imaging techniques for experimental fluid mechanics. *Annu. Rev. Fluid Mech.,* **23,** 261–304.

Al-Zanaidi, M. A., and W. H. Hui, 1984: Turbulent airflow over water waves—A numerical study. *J. Fluid Mech.,* **148,** 225–246.

Banner, M. L., 1990: The influence of wave breaking on the surface pressure distribution in wind–wave interactions. *J. Fluid Mech.,* **211,** 463–495.

——, and W. K. Melville, 1976: On the separation of airflow over water waves. *J. Fluid Mech.,* **77,** 825–842.

Batchelor, G. K., 1967: *An Introduction to Fluid Dynamics*. Cambridge University Press, 615 pp.

Belcher, S. E., 1999: Wave growth by non-separated sheltering. *Eur. J. Mech.,* **18B,** 447–462.

——, and J. C. R. Hunt, 1993: Turbulent shear flow over slowly moving waves. *J. Fluid Mech.,* **251,** 119–148.

——, J. A. Harris, and R. L. Street, 1994: Linear dynamics of wind waves in coupled turbulent air–water flow: Part 1. Theory. *J. Fluid Mech.,* **271,** 119–151.

Benjamin, T. B., 1959: Shearing flow over a wavy boundary. *J. Fluid Mech.,* **6,** 161–205.

Bolinder, J., 1999: On the accuracy of digital particle image velocimetry system. Lund Institute of Technology Division of Fluid Mechanics Tech. Rep., 24 pp.

Donelan, M. A., N. Madsen, K. K. Kahma, I. K. Tsanis, and W. M. Drennan, 1999: Apparatus for atmospheric surface layer measurements over waves. *J. Atmos. Oceanic Technol.,* **16,** 1172–1182.

——, A. V. Babanin, I. R. Young, M. L. Banner, and C. McCormick, 2005: Wave follower field measurements of the wind input spectral function. Part I: Measurements and calibrations. *J. Atmos. Oceanic Technol.,* **22,** 799–813.

——, ——, ——, ——, and ——, 2006: Wave follower field measurements of the wind input spectral function. Part II: Parameterization of the wind input. *J. Phys. Oceanogr.,* **36,** 1672–1689.

Duncan, J. H., H. Qiao, V. Philomin, and A. Wenz, 1999: Gentle spilling breakers: Crest profile evolution. *J. Fluid Mech.,* **379,** 191–222.

Elliott, J. A., 1972: Instrumentation for measuring static pressure fluctuations within the atmospheric boundary layer. *Bound.-Layer Meteor.,* **22,** 476–495.

Fabrikant, A. L., 1976: Quasilinear theory of wind waves generation. *Izv. Atmos. Ocean. Phys.,* **12,** 858–862.

Fincham, A. M., and G. R. Spedding, 1997: Low-cost, high-resolution DPIV for turbulent flows. *Exp. Fluids,* **23,** 449–462.

Gent, P. R., 1977: A numerical model of the air flow above water waves. Part 2. *J. Fluid Mech.,* **82,** 349–369.

——, and P. A. Taylor, 1976: A numerical model of the air flow above water waves. *J. Fluid Mech.,* **77,** 105–128.

Hsu, C. T., and E. Y. Hsu, 1983: On the structure of turbulent flow over a progressive water wave: Theory and experiment in a transformed wave-following coordinate system. Part 2. *J. Fluid Mech.,* **131,** 123–153.

——, ——, and R. L. Street, 1981: On the structure of turbulent flow over a progressive water wave: Theory and experiment in a transformed, wave-following co-ordinate system. *J. Fluid Mech.,* **105,** 87–117.

Ierley, G., and J. W. Miles, 2001: On Townsend's rapid distortion model of the turbulent-wind-wave problem. *J. Fluid Mech.,* **435,** 175–189.

Janssen, P. A. E. M., 1982: Quasilinear approximation for the spectrum of wind-generated water waves. *J. Fluid Mech.,* **117,** 493–506.

——, 1991: Quasi-linear theory of wind wave generation applied to wave forecasting. *J. Phys. Oceanogr.,* **21,** 1631–1642.

Jenkins, A. D., 1992: Quasi-linear eddy-viscosity model for the flux of energy and momentum to wind waves using conservation-law equations in a curvilinear coordinate system. *J. Phys. Oceanogr.,* **22,** 843–858.

Jeffreys, H., 1924: On the formation of waves by wind. *Proc. Roy. Soc. London,* **107A,** 189–206.

——, 1925: On the formation of waves by wind. II. *Proc. Roy. Soc. London,* **110A,** 341–347.

Kawai, S., 1981: Visualisation of air flow separation over wind wave crest under moderate wind. *Bound.-Layer Meteor.,* **21,** 93–104.

——, 1982: Structure of air flow separation over wind wave crest. *Bound.-Layer Meteor.,* **23,** 503–521.

Kawamura, H., and Y. Toba, 1988: Ordered motion in turbulent boundary layer over wind waves. *J. Fluid Mech.,* **197,** 105–138.

Maslowe, S. A., 1986: Critical layers in shear flows. *Annu. Rev. Fluid Mech.,* **18,** 405–432.

Melville, W. K., F. Veron, and C. J. White, 2002: The velocity field under breaking waves: Coherent structures and turbulence. *J. Fluid Mech.,* **454,** 203–233.

Miles, J. W., 1957: On the generation of surface waves by shear flow. Part I. *J. Fluid Mech.,* **3,** 185–204.

——, 1959: On the generation of surface waves by shear flows. Part II. *J. Fluid Mech.,* **6,** 568–582.

——, 1962: On the generation of surface waves by shear flow. Part IV. *J. Fluid Mech.,* **13,** 433–448.

——, 1965: On the generation of surface waves by shear flows. Part V. *J. Fluid Mech.,* **30,** 568–582.

——, 1996: Surface-wave generation: A viscoelastic model. *J. Fluid Mech.,* **322,** 131–145.

Papadimitrakis, Y. A., E. Y. Hsu, and R. L. Street, 1984: On the structure of the velocity field over progressive mechanically-generated water waves. *J. Phys. Oceanogr.,* **14,** 1937–1948.

Phillips, O. M., 1985: Spectral and statistical properties of the equilibrium range in wind-generated gravity waves. *J. Fluid Mech.,* **156,** 505–531.

——, F. L. Posner, and J. P. Hansen, 2001: High range resolution radar measurements of the speed distribution of breaking events in wind-generated ocean waves: Surface impulse and wave energy dissipation rates. *J. Phys. Oceanogr.,* **31,** 450–460.

Plant, W. J., 1982: A relationship between wind stress and wave slope. *J. Geophys. Res.,* **87,** 1961–1967.

Reul, N., H. Branger, and J.-P. Giovanangeli, 1999: Air flow separation over unsteady breaking waves. *Phys. Fluids,* **11,** 1959–1961.

——, ——, and ——, 2008: Air flow structure over short-gravity breaking water waves. *Bound.-Layer Meteor.,* **126,** 477–505.

Reutov, V. P., 1980: Plasma-hydrodynamic analogy and nonlinear stage of wind wave instability. *Izv. Atmos. Ocean. Phys.,* **16,** 938–943.

——, and Yu. I. Troitskaya, 1995: On the nonlinear effects in the interaction of gravity waves with turbulent airflow. *Izv. Atmos. Ocean. Phys.,* **31,** 825–834.

Scarano, F., and M. L. Riethmuller, 1999: Iterative multigrid approach in PIV image processing with discrete window offset. *Exp. Fluids,* **26,** 513–523.

Smolyakov, A. V., 1973: Spectrum of the quadruple radiation of the plane turbulent boundary layer. *Acoust. Phys.,* **19,** 420–425.

Sullivan, P. P., J. B. Edson, T. Hristov, and J. C. McWilliams, 2008: Large-eddy simulations and observations of atmospheric marine boundary layers above nonequilibrium surface waves. *J. Atmos. Sci.,* **65,** 1225–1245.

Valenzuela, G. R., 1976: The growth of gravity-capillary waves in a coupled shear flow. *J. Fluid Mech.,* **76,** 229–250.

van Duin, C. A., and P. A. E. M. Janssen, 1992: An analytic model of the generation of surface gravity waves by turbulent air flow. *J. Fluid Mech.,* **236,** 197–215.

Veron, F., G. Saxena, and S. K. Misra, 2007: Measurements of the viscous tangential stress in the airflow above wind waves. *Geophys. Res. Lett.,* **34,** L19603, doi:10.1029/2007GL031242.

Weissmann, M. A., 1986: Observations and measurements of air flow over water waves. *Wave Dynamics and Radio Probing of the Ocean Surface,* O. M. Phillips and K. Hasselmann, Eds., Plenum, 335–352.